



A mass-preserving interface-correction level set/ghost fluid method for modeling of three-dimensional boiling flows

B.M. Ningegowda^{a,b,*}, Zhouyang Ge^a, Giandomenico Lupo^a, Luca Brandt^{a,c}, Christophe Duwig^a

^aLinné Flow Centre and SeRC (Swedish e-Science Research Centre), KTH Mechanics, Stockholm, SE-100 44, Sweden

^bDepartment of Engineering, University of Perugia, Perugia-06125, Italy

^cDepartment of Energy and Process Engineering, Norwegian University of Science and Technology (NTNU), Trondheim-7491, Norway

ARTICLE INFO

Article history:

Received 11 May 2020

Revised 27 July 2020

Accepted 23 August 2020

Available online 2 September 2020

Keywords:

Numerical modeling

Phase change

Three-dimensional boiling flow

Level set

Global mass correction

Ghost fluid method

Interface jump

Linear extrapolation

ABSTRACT

We present an efficient method for the direct numerical simulation of three-dimensional (3D) boiling flows. The liquid-vapor interface dynamics is captured using an interface-correction level set method, modified to account for the interface heat and mass transfer due to phase change. State-of-the-art computational techniques, such as the fast pressure-correction and ghost-fluid methods, are implemented to accurately solve the coupled thermo-fluid problem involving large density contrasts and jump conditions. The solver is thoroughly validated against four benchmark cases with increasing complexity, which show better mass conservation properties than traditional level set methods, thus allowing for coarser grid resolutions and lower computational costs. We further demonstrate our method by simulating two realistic 3D boiling flows in greater details. In the first case, a saturated film boiling of water vapor at near critical conditions over a horizontal hot flat plate is considered. The results are analyzed by comparing the transient evolution of the interface morphology, temperature distribution, space and time averaged Nusselt numbers obtained from numerical simulations with the semi-empirical correlation of Berenson and existing numerical literature. In the second case, we simulate the condensation and buoyancy-driven motion of a single spherical water vapor bubble at different subcooled liquid temperatures and saturation pressures. We find opposite trends of the condensation rate and the bubble rising velocity when the degree of subcooling is increased, and an increase of the condensation rate at lower saturation pressures, due to variation of the thermophysical properties.

© 2020 Elsevier Ltd. All rights reserved.

1. Introduction

Liquid-vapor phase-change phenomena are widely encountered in industrial applications due to their high heat-transfer rates and the large energy-storage capability [1]. Examples include spray cooling and combustion, high temperature heat exchangers [2], refrigeration or cryogenic fluid thermosiphon [3], fluid storage under micro-gravity in space [4], thermal and nuclear power plants [5], cooling of electronics [6]. The successful development of these multi-scale and multi-physics technologies requires not only well-managed system engineering, but also a detailed knowledge of the underlying phase-change processes. Experimental studies of such processes are usually costly, time-consuming and demanding in

terms of operating conditions and instrument tolerance. It is therefore of paramount importance to develop accurate and efficient numerical algorithms able to capture the fluid dynamics and resolve the interfacial heat and mass transfer down to the micro-scale.

Computational methods used for multiphase flow simulations typically fall under two broad categories, i.e. reduced-order models and direct numerical simulations [7]. The former can be further divided into Eulerian-Lagrangian and Eulerian-Eulerian frameworks. In the Eulerian-Lagrangian framework, the dispersed phase (e.g. bubbles) is tracked by point forcing based on constitutive equations of mass, momentum and energy [8]. The dispersed dynamics, such as the bubble-bubble interactions, are typically modeled under the assumptions of homogeneity and spherical shape. This approach allows the explicit calculation of the bubble statistics; although topological changes such as breakup and coalescence are typically neglected. In the Eulerian-Eulerian framework, the dispersed phase is described as a field, and both the liquid and

* Corresponding author at: Linné Flow Centre and SeRC (Swedish e-Science Research Centre), KTH Mechanics, Stockholm, SE-100 44, Sweden.

E-mail address: nbm@mech.kth.se (B.M. Ningegowda).

Nomenclature

\tilde{D}	bubble diameter, m
\vec{g}	acceleration due to gravity, m/s^2
\tilde{h}_{lv}	latent heat of vaporization, J/kg
\tilde{L}	reference length scale, m
\tilde{T}	temperature, K
\tilde{U}	reference velocity, m/s
\mathbf{u}	non-dimensional velocity vector
\mathbf{g}	dimensionless gravity
k	dimensionless thermal conductivity
p	dimensionless pressure
$\mathbf{\hat{n}}$	the outward-pointing unit normal vector
\dot{m}	dimensionless interface mass flux
c_p	dimensionless specific heat at constant pressure
d	dimensionless diameter
t	dimensionless time
\mathbf{x}	position vector
\tilde{f}	any dimensional quantity, f
Fr	Froude number, $\frac{\tilde{U}^2}{\tilde{g}\tilde{L}}$
Gr	Grashof number, $\frac{g\beta\tilde{\rho}_l(\tilde{\rho}_l-\tilde{\rho}_v)\tilde{L}^3}{\tilde{\mu}_l^2}$
Ja	Jacob number, $\frac{\tilde{c}_{p,l}(\Delta\tilde{T})}{\tilde{h}_{lv}}$
Pe	Péclet number, $Re Pr$
Pr	Prandtl number, $\frac{\tilde{\mu}_l\tilde{c}_{p,l}}{\tilde{k}_l}$
Re	Reynolds number, $\frac{\tilde{\rho}_l\tilde{U}\tilde{L}}{\tilde{\mu}_l}$
We	Weber number, $\frac{\tilde{\rho}_l\tilde{U}^2\tilde{L}}{\tilde{\sigma}}$
ρ	non-dimensional density
κ	interface mean curvature
ϕ	level set function
$\tilde{\sigma}$	surface tension coefficient, N/m
μ	dimensionless dynamic viscosity
β	coefficient of thermal expansion, $1/\tilde{T}_{sat}$, $1/K$
$\Delta\tilde{T}_{sup}$	superheated temperature, $(\tilde{T}_w - \tilde{T}_{sat})$, K
$\Delta\tilde{T}_{sub}$	subcooled temperature, $(\tilde{T}_{sat} - \tilde{T}_l)$, K
ϵ	interface finite thickness, $3/2\Delta h$
$\tilde{\gamma}$	dimensional thermophysical property
$\tilde{\rho}$	dimensional density, kg/m^3
$\tilde{\mu}$	dimensional dynamic viscosity, $Pa \cdot s/m^2$
\tilde{k}	dimensional thermal conductivity, $W/m \cdot K$
\tilde{c}_p	dimensional specific heat at constant pressure, $J/kg \cdot K$
θ	non-dimensional temperature, $\frac{T-T_{ref}}{\tilde{T}_w-\tilde{T}_{ref}}$
<i>sat</i>	saturated
<i>sup</i>	superheated
<i>sub</i>	subcooled
<i>pc</i>	phase change
<i>mc</i>	mass correction
<i>c</i>	correction
<i>l</i>	liquid phase
<i>v</i>	vapor phase
<i>w</i>	wall surface
Γ	liquid-vapor interface
$n+1$	new time step
n	old time step

the bubble surface area require sophisticated modeling and are typically not valid on a general basis.

In contrast to the reduced-order descriptions, direct interface-resolved numerical simulations can capture the bubble motion and deformation down to the grid resolution. Depending on the grid generating techniques [10], these methods can be broadly grouped into (i) body fitting methods, (ii) front tracking methods, and (iii) interface capturing methods. Body fitting methods, also referred to as the Lagrangian moving body-fitted mesh approaches [11,12], are numerically complex and computationally expensive as they require frequent re-meshing to handle large topological changes. Front tracking methods (FTM) [13–16] are a semi-Lagrangian and semi-Eulerian approach where moving Lagrangian particles are tracked inside an Eulerian fixed domain. Compared to body fitting methods, the FTM are computationally less expensive, but they still require a cumbersome treatment for interface merging and fragmentation. Finally, interface capturing methods, such as the level set (LS) [17,18], the volume-of-fluid (VOF) [19–21], the coupled level set and volume-of fluid (CLSVOF) [22–26], the Volume Of fluid and level SET (VOSET) [27], and Lattice-Boltzmann Method (LBM) [28] are completely Eulerian and calculate the dynamics of the interface based on the advection of an indicator color function on a fixed grid. Compared to (i) fitting or (ii) tracking, these capturing methods are probably the easiest to implement, can automatically handle large topological changes, and are highly efficient when computed in parallel. Therefore, these capturing methods have gained increasing popularity in multiphase flow simulations, especially if breakup and coalescence are frequent. Along with the above interface capturing methods, various surface tension models have been proposed to impose the stress jump across the liquid-vapor interface. These include the continuous surface tension force (CSF) [29], continuous surface tension stress (CSS) [30], parabolic reconstruction of surface tension (PROST) [31], and ghost fluid method (GFM) [32,33]. The difference between these methods lies in the numerical treatment of the singular forcing; see Ref. [34] for a recent comparison on some of the methods and further discussions.

When heat and mass transfer occurs across the liquid-vapor interface, the energy conservation is usually modeled via Rankine - Hugoniot jump conditions [35]. In the literature, various phase change approaches have been proposed for numerical simulations of boiling flows: the sharp interface based model [23,36–38], the ghost fluid method (GFM) based model [33,35,39], and diffused model [40]. More specifically, to simulate saturated film boiling flow over a horizontal flat heater surface, various numerical methods such as FTM [1,36,41], LS [33,35,37,39], VOF [38,42–45], CLSVOF [23–25,46–48], VOSET [27,49–52] and LBM [53,54], have been reported in the literature. We note that the vast majority of these numerical studies considers mostly 2D saturated film boiling flows; only limited studies of 3D film boiling flow are carried out in [1,45]. In these works, a one-dimensional Stefan problem [38] and the saturated film boiling of a single bubble over a horizontal flat heater [36–38,42] have been widely used as the benchmark test cases. Son and Dhiri [37] simulated the LS method with 2D saturated film boiling of water and its vapor at near critical conditions of saturated pressure, $\tilde{p}_{sat} = 21.9$ MPa and saturated temperature, $\tilde{T}_{sat} = 646.15$ K.

Detailed numerical studies of complex two-phase flows with phase change, using LS/GFM and sharp interface capturing, are extensively presented in [33,35,39,55–60]. Gibou et al. [35] proposed a sharp interface capturing method using LS/GFM for the direct numerical simulation (DNS) of incompressible multiphase flows with phase change. They preserved the discontinuous nature of all the variables across the interface except for the dynamic viscosity, which was smeared with a discretized delta function. Tanguy et al. [39] presented a LS/GFM framework for capturing the in-

gas phases are solved simultaneously using separate conservation equations [9]. This approach is suitable for modeling of large-scale industrial flow, such as bubble columns. However, the closure laws for the conservation equations of mass, momentum, energy, and/or

terface motion with accurate jump conditions, for heat and mass transfer in droplet evaporation. Tanguy et al. [33] performed direct numerical simulations of boiling flows with a sharp interface formulation using the LS/GFM. The extrapolation technique of discontinuous variables is an important feature of the GFM. A thin thermal boundary layer around the bubble and the boiling mass transfer rate are accurately computed with an affordable grid resolution. They observed that a smoothed velocity jump condition at the interface can lead to erroneous mass transfer rate predictions, whereas the GFM performs better. Huber et al. [57] performed a direct numerical simulation of nucleate boiling using the LS/GFM framework at large microscopic contact angle with moderate Jakob number ($Ja < 50$) and high-density ratio. Their numerical result of bubble departure diameter shows 10% over-prediction compared to experimental data. Recently, Scapin et al. [61] proposed a VOF method for phase change problems. Lupo et al. [62] proposed a new Immersed Boundary Method (IBM) for the interface resolved simulation of spherical droplet evaporation in gas flows. Lee et al. [63] investigated the smooth distribution of the sharp phase change velocity jump condition within a finite thickness of the interface. The improved implicit mass flux projection and the post advection velocity correction step ensure the divergence-free condition of the velocity field across the interface region. In the present study, a GFM based phase change model considered similar to Tanguy et al. [33,39] to simulate the three-dimensional saturated film boiling of water and its vapor at near critical conditions of saturated pressure, $\bar{p}_{sat} = 21.9$ MPa and saturated temperature, $\bar{T}_{sat} = 646.15$ K.

Furthermore, we shall here perform a numerical simulation of 3D subcooled boiling of a single spherical bubble in a quiescent liquid to evaluate our GFM-based 3D phase change model at high densities and viscosities ratios. The subcooled boiling process occurs when the saturated or superheated vapor bubble is surrounded by a quiescent subcooled bulk liquid. Initially, the quiescent liquid is at temperature, \bar{T}_l below the saturation temperature, \bar{T}_{sat} where $\bar{T}_l < \bar{T}_{sat}$. This situation is widely encountered in light water reactors (LWRs), boiling water reactors (BWRs) and pressurized water reactors (PWRs) [64]. The safety and optimal design of water reactors depends critically on the presence of the vapor bubble which is significantly affected by the system pressure drop, rate of heat and mass transfer, and the flow stability [65]. Previous experimental studies of subcooled pool and flow boiling are presented in a number of references [66–75]. Kim and Park [71] experimentally investigated the subcooled boiling of a single bubble at low pressure and provided a correlation for the interface heat transfer coefficient as function of the local Reynolds number, Re , Prandtl number, Pr and Jacob number, Ja of the subcooled liquid phase. Lucas and Prasser [72] experimentally studied the steam-water flow in a vertical pipe using novel wire-mesh sensors for high pressure and temperature conditions. They observed that the bubble break-up is significantly influenced by the condensation process due to the change in the surface area. In these experimental studies, it is however difficult to measure the complex flow physics and heat transfer mechanism of the bubble condensation.

Numerical simulations of subcooled boiling flow can be found in the literature, using either the VOF-CSF approach based on the open source software OpenFOAM [64,76,77], a modified user defined function (UDF) in the ANSYS-FLUENT CFD software [78–80] and a geometric reconstruction of piecewise linear interface calculation (PLIC) based VOF method [81]. In particular, Jeon et al. [78] estimated the rate of bubble condensation in terms of the heat transfer coefficient at the interface obtained from the bubble velocity, liquid subcooled temperature and transient condensing spherical-bubble diameter. Bahreini et al. [76] numerically investigated the 2D single bubble dynamics with forced flow and ob-

served that the initial bubble size, liquid water subcooled temperature and inflow velocity of the bulk liquid water all play an important role for bubble deformation. Due to the velocity gradients, the condensing vapor bubble moves towards the region of higher velocity and then back to lower velocity region according the rate of subcooling. Samkhaniani and Ansari [77] accounted for the effect of (i) constant saturation temperature and (ii) local saturation temperature of the vapor bubble as a function of thermodynamic pressure which is non-uniform in quiescent subcooled water due to surface tension and acceleration due to gravity. These authors observed that for constant saturated temperature of the bubble, the bubble diameter reduces linearly due to the uniform temperature difference between the saturated vapor bubble and the subcooled liquid phase. The various bubble regimes are related to the role of the additional forces acting on the bubble such as capillary and buoyancy. Due to the condensation, the bubble reduces in size gradually and eventually collapses [82]. Numerical modeling of multiple bubble condensation is useful to understand and improve the continuum models of large scale subcooled boiling. Liu et al. [80,83] developed a geometric piecewise linear interface calculation (PLIC) based on the volume of fluid (VOF) method to simulate multiple bubble condensation. These authors observed that the rate of condensation of a single bubble can be strongly influenced by the velocity of the fluid flow and the temperature difference between the saturated bubble and the subcooled bulk liquid. In the case of multiple bubble condensation, the interaction between adjacent bubbles leads to an increase of the condensation rate of the lower bubble due to random perturbation induced by the upper surrounding bubbles. The interaction with the surrounding bubbles can be neglected if the distance between adjacent bubbles is large enough.

Sheykhi et al. [84] numerically studied the evaporation of upward saturated flow in a near-vertical tube. Toghraie [85] simulated the boiling flow of a turbulent jet impinging over a heated surface. Azadbakhti et al. [86] simulated turbulent boiling flow inside a tube with a porous medium. Recently, Molecular Dynamics Simulations (MDS) are on the rise for the investigation of boiling flows in microfluidic scenarios [87–93].

Based on the above literature review, it is observed that simulations of boiling flow models are extensively performed in 2D using LS, VOF, CLSVOF, VOSET, FTM, LBM based approaches. Further extension of these 2D phase change numerical methods for the modeling of 3D boiling flows is mathematically difficult due to the geometric reconstruction algorithm, and ends up being computationally expensive [23,45]. To avoid these issues, the LS/GFM approach is widely used for 3D boiling flows. However, the LS method with re-distancing algorithm has a known problem of mass loss, and therefore requires a very fine grid resolution with high computational cost to achieve accuracy. To overcome the mass loss issue many hybrid approaches for two-phase flow without phase change were developed, such as the global interface mass correction approach of Ge et al. [94], which is extended to phase change and further developed in the present work, to simulate 3D boiling flow problems such as saturated pool-film boiling and subcooled pool-boiling/condensation.

A projection method with a fast pressure Poisson equation solver, similar the one used by Dodd and Ferrante [95], is employed for the pressure-velocity coupling, based on fast Fourier Transforms (FFT) and Gauss elimination. To model the jump conditions for normal velocity, temperature and mass flux across interface due to phase change, the linear extrapolation technique of Aslam [96] is implemented, similarly to the efficient Ghost Fluid method (GFM) of Tanguy et al. [33,39]. The present Mass-preserving Interface Correction Level Set-Ghost Fluid Method (MICLS-GFM) based model is validated against various benchmark test cases in the literature. Simulations of 3D saturated film boiling

of near critical water over a horizontal plane heated surface and condensation of a spherical bubble in a quiescent subcooled liquid water at various operating conditions are presented and discussed.

2. Mathematical formulation

In the numerical modeling of boiling flows, the conservation of mass, momentum, and energy equations are tightly coupled to each other. These governing equations require an additional modification to account for interface jump conditions as extensively discussed in the literature [35–39]. The continuity equation is modified at the gas-liquid interface to account for the interface mass transfer, the momentum equations are modified to account for the surface tension force, viscosity jump and momentum exchange due to the phase change; finally, the energy equation is modified to account for the latent heat of vaporization [23]. In the present study, we investigate three-dimensional, unsteady, incompressible, Newtonian boiling flows.

2.1. Governing equations

In the single phase incompressible bulk fluid region, the governing equations of continuity, momentum and energy conservation are written in non-dimensional form Ge et al. [94] as

$$\nabla \cdot \mathbf{u} = 0, \quad (1)$$

$$\frac{\partial \mathbf{u}}{\partial t} + \mathbf{u} \cdot \nabla \mathbf{u} = \frac{1}{\rho_i} \left(\frac{\mu_i}{Re} \nabla^2 \mathbf{u} - \nabla p \right) + \frac{\mathbf{g}}{Fr}, \quad (2)$$

$$\frac{\partial \theta}{\partial t} + \mathbf{u} \cdot \nabla \theta = \frac{k_i}{\rho_i c_{p,i} Pe} \nabla^2 \theta, \quad (3)$$

where $\mathbf{u} = u(\mathbf{x}, t)$ is the non-dimensional velocity vector, $p = p(\mathbf{x}, t)$ is the pressure field, \mathbf{g} is a unit vector aligned with the acceleration due to gravity. The non-dimensional temperature is defined as $\theta = \left(\frac{\tilde{T} - \tilde{T}_{ref}}{\tilde{T}_w - \tilde{T}_{ref}} \right)$, where \tilde{T} is the dimensional temperature in K and the subscripts w and ref indicate the wall surface and the reference fluid phase. The non-dimensional ratios of thermophysical properties include density ρ_i , dynamic viscosity μ_i , thermal conductivity k_i and specific heat at constant pressure $c_{p,i}$. In general, the non-dimensional ratios of any thermophysical property, γ_i , is defined as the ratio of the quantity in the fluid, $\tilde{\gamma}_{c,f}$ in each cell to the corresponding reference fluid phase $\tilde{\gamma}_{ref}$.

The non-dimensional parameters of the reference fluid phase are the Reynolds number, Re is defined as the ratio of the inertia force to viscous force as $Re = \frac{\tilde{\rho}_l \tilde{U} \tilde{L}}{\tilde{\mu}_l}$, the Froude number, Fr is defined as the ratio of the flow inertia to the external gravitational field as $Fr = \frac{\tilde{U}^2}{\tilde{g} \tilde{L}}$, the Péclet number, Pe is defined as the ratio of the rate of advection of a physical quantity by the flow field to the rate of diffusion of the same quantity driven by an appropriate gradient, computed for the heat transfer as the product of the Reynolds number and the Prandtl number $Pe = Re Pr$ with the Prandtl number, Pr is defined as the ratio of momentum diffusivity to thermal diffusivity, $Pr = \frac{\tilde{\mu}_l \tilde{c}_{p,l}}{\tilde{k}_l}$. These dimensionless parameters are based on the reference length \tilde{L} , velocity \tilde{U} , time \tilde{t} , temperature \tilde{T}_{ref} , gravitational constant \tilde{g} , and the uniform thermophysical properties at the saturation condition of the reference liquid phase: density $\tilde{\rho}_l$, dynamic viscosity $\tilde{\mu}_l$, thermal conductivity \tilde{k}_l and specific heat at constant pressure $\tilde{c}_{p,l}$.¹ Subscripts v and l denote the vapor phase and the liquid phase, respectively. In the energy conservation equation, the effect of the viscous dissipation is neglected.

¹ The dimensional quantity of any variable, f is defined with a symbol tilde \tilde{f} throughout the paper.

2.2. Dimensional jump conditions

As the level-set (LS) method is a sharp interface capturing method, the governing equations are carefully discretized using various jump conditions. These jump conditions are classified into three categories: material property jump conditions, zero-order jump conditions and first order jump conditions [97]. To define the jump condition from the liquid phase, l , to the vapor phase, v , the jump operator, $[\cdot]_\Gamma$ of any quantity (e.g. f) across the interface Γ is defined [33,97] as

$$[f]_\Gamma = f_v - f_l. \quad (4)$$

The material jump conditions of the thermophysical properties, $[\tilde{\gamma}]_\Gamma$, such as density, dynamic viscosity, thermal conductivity and specific heat at constant pressure are generally written as

$$[\tilde{\gamma}]_\Gamma = \tilde{\gamma}_v - \tilde{\gamma}_l. \quad (5)$$

The enthalpy jump condition, $[h]_\Gamma = \tilde{h}_v - \tilde{h}_l$ is the latent heat of vaporization, \tilde{h}_{lv} .

The zero-order jump conditions include the jumps in the normal velocity, $\tilde{\mathbf{u}}$, and in the pressure field, \tilde{p} , across the interface Γ . The appropriate jump condition for the interface normal velocity $\tilde{\mathbf{u}}$ is expressed [33,35] in the case of phase change as:

$$[\tilde{\mathbf{u}}]_\Gamma = \dot{\tilde{m}} \left[\frac{1}{\tilde{\rho}} \right]_\Gamma \tilde{\mathbf{n}}, \quad (6)$$

where, $\dot{\tilde{m}}$ is the rate of interface mass flux in $kg/s \cdot m^2$ and $\tilde{\mathbf{n}}$ is the interface unit normal vector, directed from the liquid phase towards the vapor side of the interface. To impose the appropriate jump condition for the interfacial discontinuous pressure field, \tilde{p} one needs to consider the effect of the volumetric surface tension force, viscosity difference and momentum exchange due to interface mass transfer, $\dot{\tilde{m}}$, see also [33,35,97],

$$[\tilde{p}]_\Gamma = \tilde{\sigma} \tilde{\kappa} + 2[\tilde{\mu} \tilde{\mathbf{n}}^t \cdot \nabla \tilde{\mathbf{u}} \cdot \tilde{\mathbf{n}}]_\Gamma - \dot{\tilde{m}}^2 \left[\frac{1}{\tilde{\rho}} \right]_\Gamma, \quad (7)$$

where $\tilde{\kappa}$ is the interface mean curvature, $\tilde{\mathbf{n}}^t$ is the transpose of $\tilde{\mathbf{n}}$, and $\tilde{\sigma}$ is the surface tension coefficient in N/m , which is here assumed to be constant, though it usually depends on both temperature and concentration gradients [36]. Hence, the effect of the continuous tangential stress [37] along the liquid-vapor interface is neglected, $\nabla \tilde{\sigma} = 0$ (i.e. no Marangoni convection effect).

The first-order jump condition is referred to as Rankine-Hugoniot jump [35] and is used to account for the balance between the conservation of mass and energy across the interface. According to the first law of thermodynamics, the jump condition of the local heat flux normal to interface, $[\mathbf{q}'']_\Gamma \cdot \tilde{\mathbf{n}}$ can be written as

$$[\mathbf{q}'']_\Gamma \cdot \tilde{\mathbf{n}} = [\tilde{k} \nabla \tilde{T}]_\Gamma \cdot \tilde{\mathbf{n}}, \quad (8)$$

where the interface heat flux, $[\mathbf{q}'']_\Gamma = (q''_v - q''_l)$ is computed using Fourier's law as $[\tilde{k} \nabla \tilde{T}]_\Gamma = (-\tilde{k}_v \nabla \tilde{T}_v + \tilde{k}_l \nabla \tilde{T}_l)$ [38,43]. The interface temperature gradient of the vapor phase, $\nabla \tilde{T}_v$ and of the liquid phase, $\nabla \tilde{T}_l$ are numerically computed using second order accurate ghost linear extrapolation similar to literature [33,35,98].

Introducing the latent heat of vaporization, \tilde{h}_{lv} , the interface heat flux [33,38] can also be written as,

$$[\mathbf{q}'']_\Gamma \cdot \tilde{\mathbf{n}} = -\dot{\tilde{m}} \left(\tilde{h}_{lv} + (\tilde{c}_{p,l} - \tilde{c}_{p,v})(\tilde{T}_{sat} - \tilde{T}_\Gamma) \right) \tilde{\mathbf{n}}, \quad (9)$$

where \tilde{T}_{sat} and \tilde{T}_Γ are the saturation temperature and interface temperature in K , respectively. Various approximations have been considered to compute the interface temperature, \tilde{T}_Γ ; among those, a Dirichlet boundary condition with constant saturation temperature of $\tilde{T}_\Gamma = \tilde{T}_{sat}$ is widely imposed [23,36–38,43,46].

Based on the uniform saturation condition at the interface, the mass flux normal to the interface is simplified to [43]

$$\dot{m} = -\frac{(-\tilde{k}_v \nabla \tilde{T}_v + \tilde{k}_l \nabla \tilde{T}_l)}{\tilde{h}_{lv}} \cdot \tilde{\mathbf{n}}. \quad (10)$$

Using a whole domain (or single-fluid) formulation similar to Huber et al. [57], the energy conservation equation with latent heat transfer due to phase change is written as:

$$\tilde{\rho} \tilde{c}_p \left(\frac{\partial \tilde{T}}{\partial \tilde{t}} + \tilde{\mathbf{u}} \cdot \nabla \tilde{T} \right) = \nabla \cdot (\tilde{k} \nabla \tilde{T}) - \dot{m} \tilde{h}_{lv} \delta_\Gamma. \quad (11)$$

On the discrete level, the above energy equation is solved temporally using a three-stage total-variation-diminishing (TVD) third order Runge-Kutta (RK-3) scheme [94] and spatially using a Fifth order High-Order Upstream-Central (HOUC-5) scheme [99]. The diffusion term is discretized by the typical second order Central Differencing (CD-2) scheme, and the jump conditions of temperature and mass flux across the interface is considered using the PDE based linear extrapolation approach [33,96].

2.3. Interface heat and mass transfer model

In the phase change model, the mass jump condition, \dot{m} across the interface is written as

$$\dot{m} = [\tilde{\rho}(\tilde{\mathbf{u}} - \tilde{\mathbf{u}}_{int})]_\Gamma \cdot \tilde{\mathbf{n}} = 0, \quad (12)$$

and the jump condition of the energy across the interface, Γ is

$$[\tilde{\rho} \tilde{h}(\tilde{\mathbf{u}} - \tilde{\mathbf{u}}_{int})]_\Gamma \cdot \tilde{\mathbf{n}} = -[q'']_\Gamma \cdot \tilde{\mathbf{n}}, \quad (13)$$

where $[q'']_\Gamma \cdot \tilde{\mathbf{n}} = (q''_v - q''_l) \cdot \tilde{\mathbf{n}}$ is the net conduction heat flux across the liquid-vapor interface. Based on the balance between mass and energy jump conditions, the interfacial mass flux, \dot{m} can be rewritten as

$$\dot{m} = \frac{-[q'']_\Gamma \cdot \tilde{\mathbf{n}}}{\tilde{h}_{lv}}. \quad (14)$$

Due to the interface phase change, the interface normal velocity field, $[\tilde{\mathbf{u}}]_\Gamma = (\tilde{\mathbf{u}} - \tilde{\mathbf{u}}_{int}) \cdot \tilde{\mathbf{n}}$ is computed across the interface as

$$[\tilde{\mathbf{u}}]_\Gamma = \dot{m} \cdot \tilde{\mathbf{n}} \left[\frac{1}{\tilde{\rho}} \right]_\Gamma, \quad (15)$$

where the reciprocal of the density jump condition, $\left[\frac{1}{\tilde{\rho}} \right]_\Gamma$ is calculated as $\left(\frac{1}{\tilde{\rho}_v} - \frac{1}{\tilde{\rho}_l} \right)$.

Re-writing the mass flux, \dot{m} in (Eq. (15)) using $\tilde{\mathbf{u}}_{int}$ in the moving reference frame, viz.

$$\dot{m} = \tilde{\rho}_l (\tilde{\mathbf{u}}_l - \tilde{\mathbf{u}}_{int}) \cdot \tilde{\mathbf{n}} = \tilde{\rho}_v (\tilde{\mathbf{u}}_v - \tilde{\mathbf{u}}_{int}) \cdot \tilde{\mathbf{n}}, \quad (16)$$

The velocity front, $\tilde{\mathbf{u}}_{int}$, defining the transient evolution of the interface in the moving reference frame, becomes

$$\tilde{\mathbf{u}}_{int} = \tilde{\mathbf{u}}_l - \frac{\dot{m}}{\tilde{\rho}_l} \tilde{\mathbf{n}} = \tilde{\mathbf{u}}_v - \frac{\dot{m}}{\tilde{\rho}_v} \tilde{\mathbf{n}}. \quad (17)$$

2.4. Modified non-dimensional jump conditions

The non-dimensional form of the interface mass flux, \dot{m} in Eq. (10), is expressed by Luo et al. [100] as

$$\dot{m} = \frac{Ja}{Pe} (k_i \nabla \theta_v - \nabla \theta_l) \cdot \tilde{\mathbf{n}}, \quad (18)$$

where θ is the non-dimensional temperature, and the Jacob or Jakob number, Ja , is defined as the ratio of sensible heat to latent heat absorbed (or released) during the phase change process with

respect to the reference phase, $Ja = \frac{c_{p,l} \Delta \tilde{T}_{ref}}{\tilde{h}_{lv}}$. The interfacial temperature gradient, $\nabla \theta$, is calculated with a second-order accurate ghost linear extrapolation similar to Tanguy et al. [33], Gibou et al. [35].

The dimensionless form of the interface normal velocity, $[\mathbf{u}]_\Gamma$, is written as

$$[\mathbf{u}]_\Gamma = \dot{m} \cdot \tilde{\mathbf{n}} \frac{1 - \rho_i}{\rho_i} = \frac{1 - \rho_i}{\rho_i} \frac{Ja}{Pe} (k_i \nabla \theta_v - \nabla \theta_l) \cdot \tilde{\mathbf{n}}, \quad (19)$$

whereas the dimensionless form of the conservation of mass across the interface region is [100]

$$\nabla \cdot \mathbf{u} = \frac{1 - \rho_i}{\rho_i} \frac{Ja}{Pe} (k_i \nabla \theta_v - \nabla \theta_l) \cdot \tilde{\mathbf{n}}. \quad (20)$$

The interfacial pressure jump condition of Eq. (7), becomes in non-dimensional form Luo et al. [100]:

$$[p]_\Gamma = \frac{\kappa}{We} + \frac{2}{Re} [\mu \mathbf{n}^t \cdot \nabla \mathbf{u} \cdot \mathbf{n}]_\Gamma - \left(\frac{Ja}{Pe} (k_i \nabla \theta_v - \nabla \theta_l) \right)^2 \frac{1 - \rho_i}{\rho_i}, \quad (21)$$

where κ is the dimensionless mean curvature of the interface [94]. The Weber number, We is the ratio of inertial forces to surface tension forces and is defined as $We = \frac{\tilde{\rho}_l \tilde{U}^2 \tilde{L}}{\tilde{\sigma}}$. The normal derivative of the discontinuous interface velocity due to the phase change process is accounted using a simple ghost velocity extension approach similar to Tanguy et al. [33].

2.5. The classical level set method

In the current numerical framework, we advect the liquid-vapor interface using a modified version of the mass-preserving interface-correction level set method (MCLS) that was originally proposed in [94]. In the classical LS method [17,101], the moving interface is represented as the zero iso-contour of a shortest-distance function $\phi(\mathbf{x}, t)$, i.e. $\Gamma = \{\mathbf{x} \mid \phi(\mathbf{x}, t) = 0\}$. In the liquid phase, the LS function is defined as the positive distance to the interface, $\phi(\mathbf{x}, t) = +d$, whereas in the discrete vapor-phase region, the LS function is negative, $\phi(\mathbf{x}, t) = -d$. The advection equation for ϕ in the case of phase change problems is written as [33,35,37]

$$\frac{\partial \phi}{\partial t} + \mathbf{u}_\Gamma \cdot \nabla \phi = 0, \quad (22)$$

where \mathbf{u}_Γ is the dimensionless velocity of the moving front and is defined using Eq. (17) as

$$\mathbf{u}_\Gamma = \mathbf{u}_l - \frac{\dot{m}}{\rho_l} \tilde{\mathbf{n}} = \mathbf{u}_v - \frac{\dot{m}}{\rho_v} \tilde{\mathbf{n}}. \quad (23)$$

Note that the underlying velocity field is discontinuous across the interface, see Eq. (15). Due to the non-uniform advection velocity, ϕ will therefore lose its regularity over time. To ensure numerical stability and accuracy, it is customary to regularly reshape ϕ into the signed distance function by solving the following Hamilton-Jacobi equation [102]

$$\frac{\partial \phi}{\partial \tau} + S(\phi_0) (|\nabla \phi| - 1) = 0, \quad (24)$$

where τ is the pseudo-time, and $S(\phi_0)$ is the mollified sign function (see e.g. [94] for its definition). Eq. (24) is typically iterated once per ten physical time steps. The numerical schemes for solving Eqs. (22), (24) are the same as in [94]. Specifically, we use a third-order Runge-Kutta (RK-3) scheme for the temporal integration, a fifth-order Higher Order Upstream Central (HOUC-5) scheme [99] for the convective terms in Eq. (22), and a fifth-order weighted essentially non-oscillatory (WENO-5) scheme for the spatial discretizations in Eq. (24).

In the LS method, the unit normal vector, \vec{n} , and the interface mean curvature, κ , can be readily computed from the level set function

$$\vec{n} = \frac{\nabla \phi}{|\nabla \phi|}, \quad \kappa = -\nabla \cdot \vec{n}. \quad (25)$$

The thermophysical properties, $\gamma(\rho, \mu, k, c_p)$, can be written as

$$\gamma(\phi) = \gamma_l H(\phi) + \gamma_v (1 - H(\phi)), \quad (26)$$

where $H(\phi)$ is a smoothed Heaviside function obtained from the continuous LS function, ϕ as

$$H(\phi) = \begin{cases} 1 & \text{if } \phi > \epsilon, \\ \frac{1}{2} + \frac{\phi}{2\epsilon} + \frac{1}{2\pi} \sin\left(\frac{\pi\phi}{\epsilon}\right) & \text{if } |\phi| \leq \epsilon, \\ 0 & \text{if } \phi < -\epsilon. \end{cases} \quad (27)$$

For a uniform grid spacing, Δh , the interface is assumed to have finite thickness $\epsilon = \frac{3}{2}\Delta h$. The Heaviside function, $H(\phi)$ effectively smears the discontinuity across the liquid-vapor interface, avoiding numerical instability [103].

Solving both LS advection and re-distancing does not guarantee mass conservation [82,104,105] due to the numerical errors arising in the discretization schemes. To overcome this problem, various global mass correction schemes have been proposed [82,94,105]. Here, the interface correction LS (ICLS) method of [94] is modified to simulate 3D phase change problems.

2.6. MICLS-based global mass correction method

The main advantages of the level set method are its simplicity and accurate curvature calculation, which reduces erroneous velocities and spurious currents [19,29] commonly occurring in interface capturing methods [94,106]. The disadvantage, however, is the inherent mass loss when applied to incompressible, multi-phase flows. As discussed earlier, many efforts have been devoted to overcoming the issue of mass loss by e.g. coupling with the VOF method, so called CLSVOF [23] and VOSET [27] methods. Note, however, that the geometric reconstruction and advection procedure of the VOF method becomes numerically difficult and computationally expensive for 3D problems [20,21].

In this study, the MICLS is applied across the finite thickness of the interface region to obtain global mass conservation for boiling flows. To improve the LS method to conserve mass, the interface velocity correction approach of [94] is extended to phase change processes. The modifications proposed here take into account the velocity jump due to phase change, while maintaining the simplicity of the standard level set method. The detailed algorithm is described below. This velocity correction is not required at every time step and has a limited computational cost. The interface velocity correction is based on the solution of a PDE as for the LS advection equation.

As in [94], we solve an additional advection equation to compensate the mass loss, viz.

$$\frac{\partial \phi}{\partial t} + \mathbf{u}_c \cdot \nabla \phi = 0, \quad (28)$$

where \mathbf{u}_c is the interface correction velocity field, satisfying

$$\int_{\Gamma} \vec{n} \cdot \mathbf{u}_c d\Gamma = \frac{\delta V}{\delta t}. \quad (29)$$

Here, $\delta V/\delta t$ denotes the dispersed volume (e.g. bubbles) that is numerically lost over some time. Since the bubble volume can change physically due to boiling or condensation, the actual rate of mass loss at time n is

$$\left(\frac{\delta V}{\delta t}\right)^{(n)} = \frac{(V^{(n)} - V^{(n-N_{mc})}) - \delta V_{pc}^{(n)}}{N_{mc} \Delta t}, \quad (30)$$

where $\delta V_{pc}^{(n)}$ is the volume change due to phase change at time level n , and N_{mc} is the number of time steps between each correction, solution of Eq. (28). Here, we choose $N_{mc} = 20$, that is, we perform the mass correction every 20 physical time steps.

In Eq. (30), $V^{(n)}$ and $V^{(n-N_{mc})}$ can be obtained easily by integrating the Heaviside function, Eq. (27), over the whole domain, e.g.

$$V^{(n)} = \int_{\Omega} (1 - H(\phi^{(n)})) d\Omega. \quad (31)$$

$\delta V_{pc}^{(n)}$ depends on the integral of the interface velocity, from the last time the mass correction was performed to the present time, i.e.

$$\delta V_{pc}^{(n)} = \int_{t^{(n-N_{mc})}}^{t^{(n)}} \int_{\Gamma} \vec{n} \cdot \mathbf{u}_{\Gamma} d\Gamma dt'. \quad (32)$$

Numerically, the surface integral in Eq. (32) can be approximated by the sum of the interface velocity multiplied by a Dirac delta function,

$$\int_{\Gamma} \vec{n} \cdot \mathbf{u}_{\Gamma} d\Gamma \simeq \sum (\vec{n} \cdot \mathbf{u}_{\Gamma}) \delta(\phi) \Delta x \Delta y \Delta z \quad (33)$$

where $\delta(\phi)$ is the derivative of Eq. (27)

$$\delta_{\epsilon}(\phi) = \begin{cases} 0 & \text{if } \phi > \epsilon \\ \frac{1}{2\epsilon} (1 + \cos(\frac{\pi\phi}{\epsilon})) & \text{if } |\phi| \leq \epsilon \\ 0 & \text{if } \phi < -\epsilon \end{cases}$$

Finally, the algebraic form of the correction velocity is expressed in the same way as in [94],

$$\mathbf{u}_c(\phi) = \frac{\delta V}{\delta t} \frac{\kappa(\phi)}{A_{\Gamma}} \nabla H(\phi), \quad (34)$$

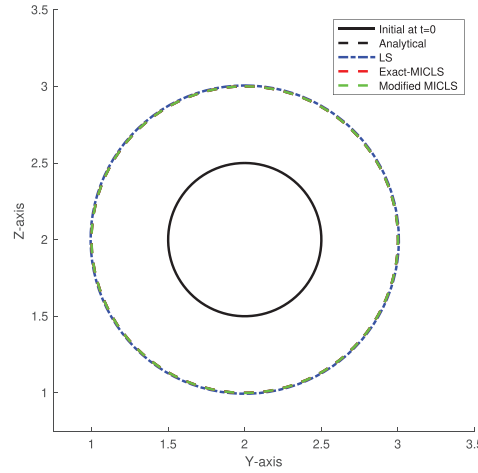
where $A_{\Gamma} = \int_{\Gamma} \kappa(\phi) \delta(\phi) |\nabla \phi| d\Gamma$. The interface correction velocity \mathbf{u}_c becomes large for highly curved interfaces, because the local information of the interface is used to obtain the global mass conservation. The mass correction is used to correct the LS function near the interface, before the LS re-initialization is performed.

3. Numerical model validations

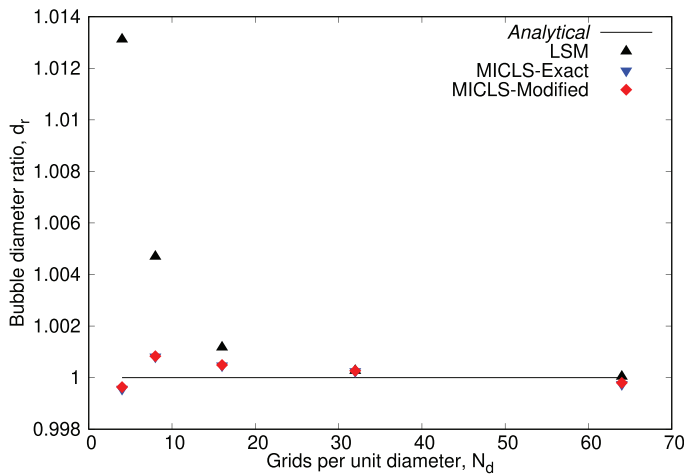
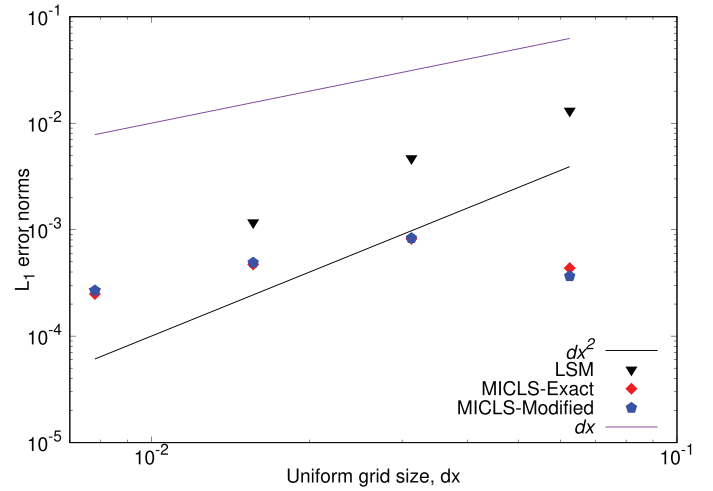
The ICLS method was extensively validated by Ge et al. [94] for simulating 3D two-phase flows without phase change. Here, we present validations for flows with phase change. In the numerical verifications of the present model, we consider (i) the LS advection, re-distancing and modified LS mass correction algorithm of [94], (ii) a linear ghost extrapolation of the non-divergence free velocity field as in [33], (iii) a second order accurate extrapolation of the temperature as in [96,98] and (iv) a second order extrapolation of the phase-change mass flux [33] across the finite thickness of the interface region.

3.1. Evaluation of the LS advection algorithm

Here, a simple analytical benchmark test case is used to evaluate the LS advection, re-initialization and MICLS based mass correction algorithms for simulating two-phase flows with phase change. We consider a spherical bubble undergoing uniform expansion as discussed in [33,107]. In detail, an initially spherical gas bubble linearly expands by an externally-imposed constant interface mass flux, with uniform interface normal velocity, $[u]_{\Gamma} = 0.1$. This test case does not require the solution of the Navier-Stokes and energy equations, only of the LS-related algorithms. Also, the effects of the thermophysical properties of the working fluids and the acceleration due to gravity are neglected. Initially, a zero velocity field is imposed in the whole computational domain. The evolution of the dimensionless spherical bubble diameter, $d(t)$ function of the non-dimensional time, t is given by $d(t) = d(0) + [u]_{\Gamma} t$.



(a) Bubble radius at grid resolution of 1/8

(b) Bubble diameter ratio, d_r 

(c) Absolute error

Fig. 1. Grid resolution study for the test case of uniform expansion of a spherical bubble.

where, $d(0) = 1$ is the initial dimensionless bubble diameter. In the simulations, we consider the spherical bubble at the centre of a cubic domain of length, $l = 4d(0)$. The cubic domain is uniformly discretized using an increasing grid resolution of 16^3 , 32^3 , 64^3 , 128^3 and 256^3 , with corresponding grid size, $\Delta h = d(0)/N_d = 1/4$, $1/8$, $1/16$, $1/32$ and $1/64$. A constant time step of $\Delta t = 10^{-3}$ is used.

The non-dimensional spherical bubble diameter at dimensionless time, $t = 5$ obtained from three different algorithms is compared with the exact analytical solution in Fig. 1. In particular, we consider a classical LS method implementation (denoted LSM), an interface-correction level set using the analytically known exact volume (MICLS-Exact) and the same approach with corrections obtained integrating from the interface normal velocity (MICLS-Modified). A simple visualization like that in panel a) does not enable us to differentiate the various mass corrections even for the coarse grid resolution of $\Delta h = 1/8$. Hence, we report in panel b) of the same figure the ratio between the bubble diameter at $t = 5$ from the simulations and the theoretical value, $d_r = d(t)_{num}/d(t)_{exact}$, for the different resolutions considered. The data show that the correct and modified MICLS well approximate the exact solution already at low resolution (4 and 8 grid points per bubble diameter), whereas a classic LS would require 32 points to achieve a similar accuracy. For a simple test case like this one, the

present LS advection with mass correction algorithms becomes independent of the grid resolution unlike classical LS without mass correction.

The absolute error or L_1 error norm is the difference between the computed value and true value, is defined here as $E = |d(t)_{num} - d(t)_{exact}|$, is reported in Fig. 1(c) for the different grid resolutions under investigation in logarithmic scale. The error at final time at $t = 5$ from the different implementations indicates that the order of convergence for the classical LS method without mass correction varies between first and second. The LS method with MICLS based mass correction displays an order of convergence between first and second for the coarser grids and close to second order accuracy for finer grids. Hence, the LS method with MICLS based mass correction is able to conserve mass already at coarse grid resolution, which implies a lower computational cost than for the classical LS method.

3.2. Non-divergence free Interface velocity

In our approach, the modified momentum equations for the simulation of phase change are modeled similarly to the non-divergence free conditions with the interface velocity extension approach considered by Tanguy et al. [33]. In this new test, the pre-

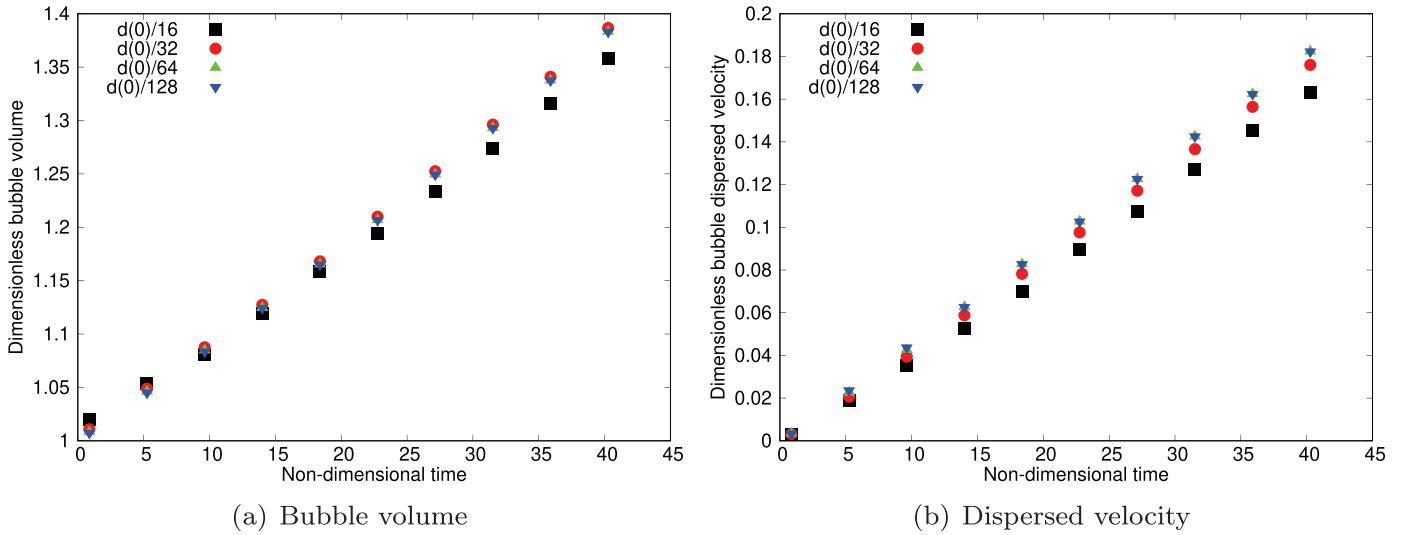


Fig. 2. Uniform expansion of a spherical bubble at constant mass rate. Expanding bubble volume and dispersed bubble velocity for the different grid resolutions examined.

viously evaluated MICLS advection algorithm is merged with the projection method to obtain the pressure and velocity coupling. We still consider the case of a uniformly expanding spherical bubble in the absence of gravity, a case which does not require the solution of the energy equation. The growth of the spherical bubble is due to the imposed uniform mass transfer rate and the non-divergence free condition of the simple velocity extension is considered within an interface region of finite thickness, $\pm 6\Delta h$.

Tanguy et al. [33] performed a 2D simulation of this problem with a dimensional reference bubble diameter of $\tilde{D} = 0.002m$ placed at the center of a square domain of length $\tilde{L} = 4\tilde{D}$. Following these previous studies [33,39], we assume the physical properties of liquid water and air at 1atm with density of liquid, $\rho_l = 1000 \text{ kg/m}^3$, density of gas, $\rho_v = 1 \text{ kg/m}^3$, dynamic viscosity of liquid, $\mu_l = 1.0 \times 10^{-3} \text{ kg/ms}$ and dynamic viscosity of gas, $\mu_v = 1.78 \times 10^{-5} \text{ kg/ms}$, with a constant surface tension coefficient of $\sigma = 0.07 \text{ N/m}$ and uniform mass transfer rate of $0.1 \text{ kg m}^{-2} \text{ s}^{-1}$.

Here, we present a 3D validation on a cubic computational domain discretized using a uniform mesh with 64^3 , 128^3 , 256^3 and 512^3 grid points, corresponding to a grid size Δh in units of the initial bubble diameter, $d(0)/N_d = 1/16$, $1/32$, $1/64$ and $1/128$. Periodic boundary conditions are imposed in the x and y directions and homogeneous Neumann boundary conditions on the top and bottom boundaries. The constant time step is $\Delta t = 1.0 \times 10^{-6}$ owing to the high density and dynamic viscosities ratios, $\rho = 1.0 \times 10^{-3}$ and $\mu = 1.78 \times 10^{-2}$. The non-dimensional parameters defining the test case are based on a reference length equal to the initial bubble diameter, $\tilde{L} = \tilde{D}$ is $0.002m$, reference velocity, $\tilde{U} = \sqrt{\tilde{D}\tilde{g}} = 0.14m/s$ and reference time scale, $\tilde{t} = \tilde{D}/\tilde{U} = 0.01427s$. Using the liquid as the reference phase, the Reynolds number is $Re = 280$ and the Weber number is $We = 0.56$. Here, the qualitative comparison is carried out in terms of averaged bubble dispersed velocity, u_{disp} , defined as

$$u_{disp} = \sqrt{u(x)^2 + u(y)^2 + u(z)^2}, \quad (35)$$

and reported in terms of $u_d = u_{disp}/\tilde{U}$. The time evolution of the non-dimensional expanding bubble volume, $V(t)$, and of the dimensionless bubble dispersed velocity, u_d are displayed in Fig. 2(a) and (b) for the different grid sizes under consideration. The results show that for the fine grid size, Δh smaller than $1/32$, both the bubble volume and the average dispersed velocity obtained from the present MICLS method becomes independent of the grid resolution. Deviations are observed for the coarse grid resolution

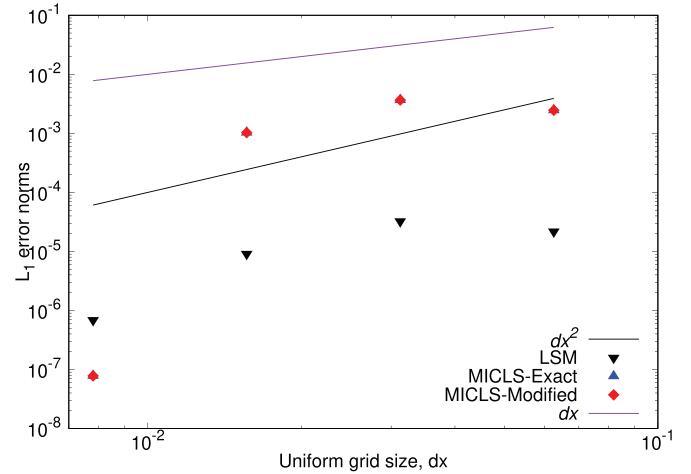


Fig. 3. Absolute error versus grid resolution for the test case of a bubble expanding at constant mass transfer rate.

of $1/16$. To accurately capture the interface dynamics and flow physics, a minimum grid size per unit bubble diameter of $\Delta h = 1/32$ is therefore required.

The order of convergence, defined by the absolute or L_1 error norm at the various grid resolutions, is shown in Fig. 3. Recalling that the order of convergence of the LS with mass correction is between first and second order, see Fig. 1(c), coupling the LS advection with mass correction (MICLS) with the projection method reduces it to first order accurate. However, the simple interface ghost velocity extension of the present 3D problem is computationally cheaper than the 3D extension in Tanguy et al. [33], due to the iterative solution at each time step of a Poisson equation for the ghost velocity extension. This requires approximately twice the computational cost than without the ghost velocity extension [37].

3.3. Extrapolated interface temperature for two-phase flows

At the liquid-vapor interface, both temperature and heat flux are continuous and are written as $\tilde{T}_\Gamma = \tilde{T}_{\Gamma,l} = \tilde{T}_{\Gamma,v}$ and $q''_\Gamma = q''_{\Gamma,l} = q''_{\Gamma,v}$, respectively. The local heat flux, $q'' = -\tilde{k}\nabla\tilde{T}_n$ is computed using Fourier's law of heat conduction. The temperature gradient,

$\nabla \tilde{T}_n$ is therefore discontinuous across the interface and should be computed independently from either side of the liquid-vapor interface [43,45]. In the literature of piecewise linear interface calculation based volume of fluid (PLIC-VOF) method [23,43,45], the liquid-vapor interface is approximated as a flat plane in the computational cell, leading to the following energy balance as

$$-\tilde{k}_v \frac{\tilde{T}_\Gamma - \tilde{T}_v}{\Delta n_v} = -\tilde{k}_l \frac{\tilde{T}_\Gamma - \tilde{T}_l}{\Delta n_l}, \quad (36)$$

where Δn denotes the distance to from a nodal point to the interface in the normal direction. From the above relation, the 1D interfacial temperature for the two-phase flow is written as

$$\tilde{T}_\Gamma = \frac{\tilde{k}_v \tilde{T}_v \Delta n_l + \tilde{k}_l \tilde{T}_l \Delta n_v}{\tilde{k}_v \Delta n_l + \tilde{k}_l \Delta n_v}, \quad (37)$$

which becomes in dimensionless form, θ ,

$$\theta_\Gamma = \frac{k_l \theta_v \Delta n_l + \theta_l \Delta n_v}{k_l \Delta n_l + \Delta n_v}. \quad (38)$$

This interpolation provides the fixed interface temperature, which is also the saturation temperature at the system pressure. However, to extend this simple 1D interpolation approach of temperature Eq. (38) into numerical study of 2D or 3D problems is generally difficult. Hence, PDE based ghost extrapolations such as constant, linear and quadratic approaches are proposed in the literature [33,35,96] to accurately solve the heat flux normal to the interface for 3D problems. The main advantage of these ghost extrapolation approaches is that both momentum and energy equations are solved independently in the liquid phase and vapor phase similar to Tanguy et al. [33].

In the present numerical study, the PDE based second-order ghost linear extrapolation is adopted, similarly to Aslam [96] and Tanguy et al. [33]. Here, the linear extrapolation of non-dimensional temperature, θ is considered based on following procedures. In first step, the directional derivative of temperature in the normal direction, θ_n is defined in the region where temperature, θ is known in one phase with LS function, $\phi \leq 0$ as

$$\frac{\partial \theta}{\partial n} = n \cdot \nabla \theta. \quad (39)$$

In second step, the above scalar function can be extrapolated in another phase region, $\phi > 0$ via PDE with following expression as

$$\frac{\partial \theta_n}{\partial \tau} + H(\phi) n \cdot \nabla \theta_n = 0. \quad (40)$$

This equation is solved until it reaches the steady state, where the characteristic wave speed is unity and steady PDE becomes $n \cdot \nabla \theta_n = 0$. Finally, after solved the directional derivative everywhere in the region, $\phi > 0$, then we solve the non-dimensional temperature, θ as

$$\frac{\partial \theta}{\partial \tau} + H(\phi) (n \cdot \nabla \theta - \theta_n) = 0. \quad (41)$$

Here, the Heaviside function, $H(\phi)$ is used to not disturb the known values of temperature in the region, $\phi \leq 0$. In the GFM, a narrow band of points near the interface is used to populate ghost cells.

To validate the linear extrapolation of the temperature across the interface, a simple plane interface with 1D steady state is solved similar to test case considered by Son and Dhir [82]. Here, a 3D unsteady, laminar, two-phase flow with heat transfer without phase change process is used to obtain the 1D steady state solution. From this steady state solution, the linear temperature variations inside the superheated vapor phase and subcooled liquid phase are obtained and compared with the temperature profile of the analytical solution.

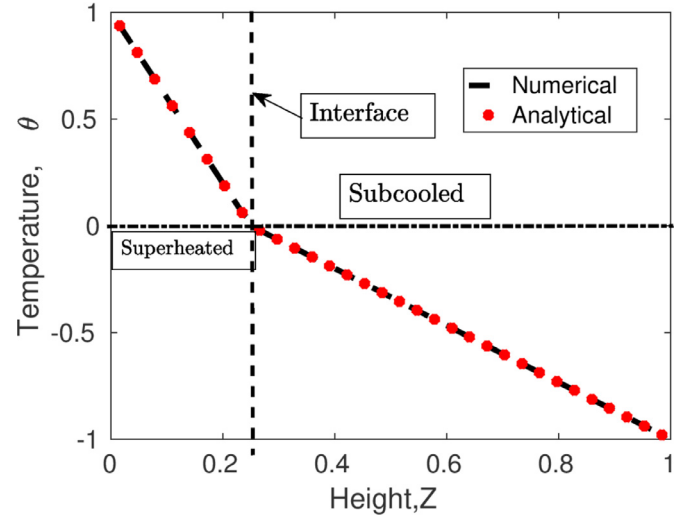


Fig. 4. 1D Steady solution of the two-phase flow with heat transfer without phase change.

In our test, a plane interface with non-dimensional film thickness of height, $\delta = 0.25$ is placed inside a unit cube computational domain. The domain is discretized with a uniform grid size of 128^3 , with periodic boundary conditions imposed in both X and Y directions. The bottom boundary consists of a no-slip wall with superheated non-dimensional temperature, $\theta_w = 1$ imposed as Dirichlet condition, whereas the top boundary is a no-slip wall with the subcooled non-dimensional temperature $\theta_w = -1$. Initially, both phases are at saturation temperature, $\theta = 0$, with zero velocity in the whole domain. The unsteady temperature equation is solved independently in the liquid and vapor phase similarly to the ghost extrapolation approach of [33,57] and the numerical simulation carried out until the steady state solution is reached. The temperature variations inside both superheated vapor and subcooled liquid water at its near critical conditions of $\tilde{p}_{sat} = 219 \text{ bar}$ and $\tilde{T}_{sat} = 646.15 \text{ K}$ are considered. The comparison of the linear temperature obtained from the numerical and analytical solution is shown in Fig. 4. The good agreement in the figure indicates the PDE-based second-order accurate linear ghost temperature extrapolation can be further used to simulate 3D two-phase flows with heat and mass transfer.

3.4. Ghost fluid method (GFM) based phase change model

Next, we examine the ghost fluid method (GFM) for interface heat and mass transfer. The present GFM model is validated against the benchmark case of the one-dimensional Stefan problem considered in [23,35,38,42]. In this test, the interface normal velocity due to the phase change is varying non-uniformly both temporally and spatially and it is calculated based on the temperature gradient across the finite thickness of the interface.

We compare the transient evolution of the plane interface thickness obtained from the present numerical study with the analytical solution of the 1D Stefan problem. Here, we consider constant thermophysical properties of liquid water and its vapor at near critical conditions of $\tilde{p}_{sat} = 219 \text{ bar}$ and $\tilde{T}_{sat} = 646.15 \text{ K}$ as in [24,46]. The non-dimensional variables are based on the capillary length computed with constant thermo-physical properties [1]. A film of initial thickness $\delta = 0.15$ is placed inside the unit-cube computational domain shown in Fig. 5(a). The 3D computational domain is uniformly discretized using a grid size of 128^3 and the simulations run with a uniform time step $\Delta t = 10^{-5}$. Periodic boundary conditions are imposed in the wall-parallel plane.

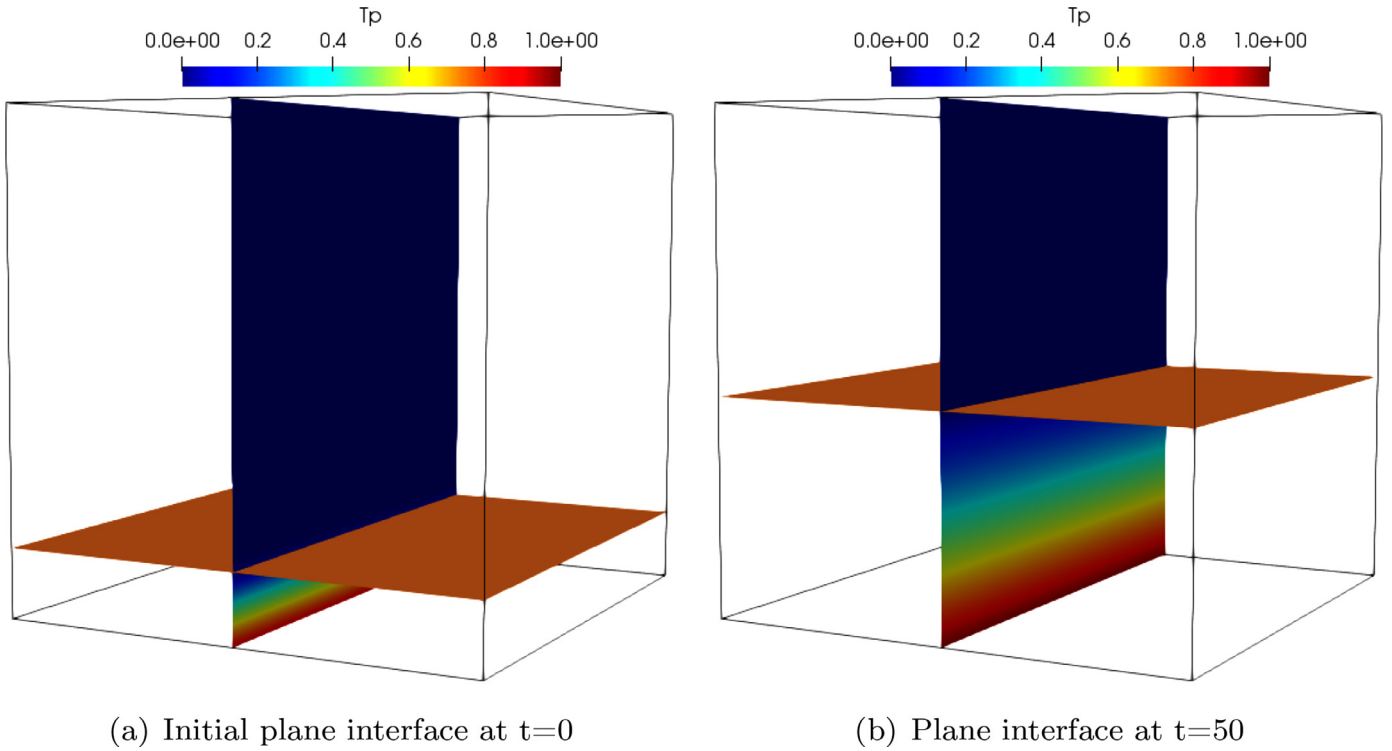


Fig. 5. Visualization of the interface at different instants from the numerical solution of the 1D Stefan problem with non-uniform phase change.

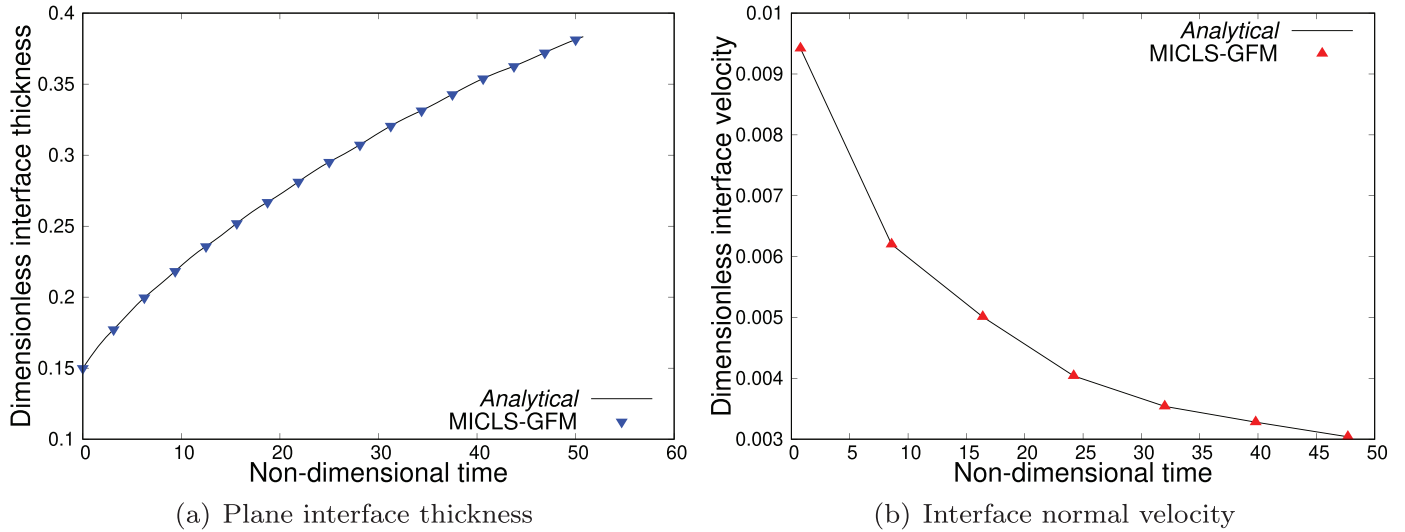


Fig. 6. The transient evolution of the interface thickness and velocity field for the 1D Stefan problem.

The bottom boundary is a no-slip wall at superheated temperature $\Delta \tilde{T}_{sup} = 25K$ and corresponding dimensionless temperature $\theta_w = 1$, whereas the top boundary is a zero gradient/open boundary. Initially, liquid is at saturated condition, $\theta = 0$, and a linear temperature profile is initialized in the thin layer of vapor at the superheated bottom wall. The initial velocity field is set to zero in the whole domain. Continuous heat transfer takes place between the superheated bottom wall and the adjacent quiescent vapor phase so that a thermal boundary layer develops inside the vapor region which drives the plane interface upwards due to heat and mass transfer normal to the interface, see Fig. 5(b).

The transient evolution of the plane interface thickness and the corresponding interface normal velocity obtained from the present 3D MICLS-GFM based phase change are reported in Fig. 6(a) and

(b). Both the interface film thickness and normal velocity display close agreement with the analytical solution. Concluding, the present GFM based interface heat and mass transfer model can be used to capture the flow physics and heat transfer rate for 3D boiling flows.

4. Simulations of three-dimensional boiling flows

The GFM based phase change model considered in the present numerical study is further validated using 3D boiling flows such as saturated film boiling over a horizontal plane surface [1] and subcooled boiling of a spherical vapor bubble inside a quiescent liquid column [76].

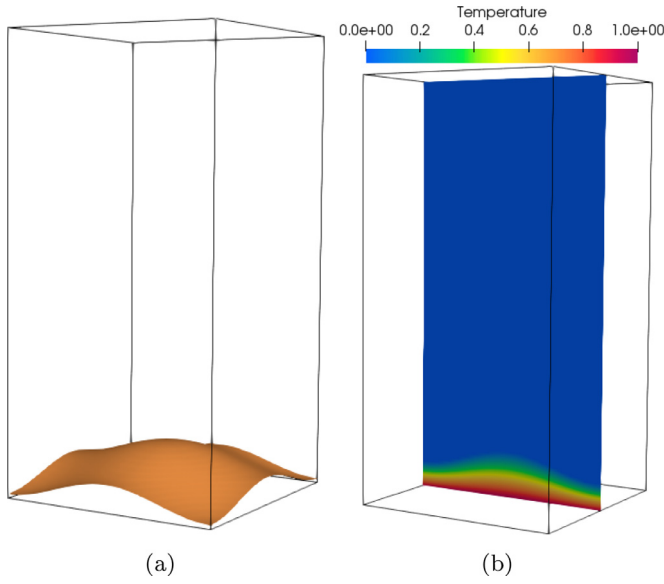


Fig. 7. Initial condition for the simulation of 3D film boiling. (a) Thin vapor film thickness and (b) Linear temperature profile.

4.1. Saturated 3D film boiling

Even though the surface heat transfer rate obtained from nucleate boiling is higher and most favourable for industrial applications, studies of film boiling are carried out in the literature mostly to understand the accidental situations encountered in industrial reactors and boilers [1]. Here, we simulate a single-mode (one bubble dynamics) saturated film boiling of water over a horizontal plane surface. A thin layer of vapor film completely covers a superheated flat surface and the mass transfer takes place at the liquid-vapor interface, see initial configuration in Fig. 7. This thin vapor layer acts as a blanketed insulating layer between the heated surface and the quiescent saturated liquid. As above, periodic boundary conditions are imposed in the wall-parallel directions whereas the bottom boundary is a no-slip wall with uniform superheated temperature $\tilde{T}_w = \tilde{T}_{sat} + \Delta\tilde{T}_{sup}$ and corresponding non-dimensional temperature of $\theta_{sup} = 1$. At the top boundary, we impose outflow conditions with zero temperature gradient. Due to the evaporation of the liquid, the liquid-vapor interface becomes unstable and a bubble is generated. The spherical vapor bubble grows in size, detaches from the interface and rises upwards due to buoyancy.

In our numerical simulations, constant thermophysical properties are assumed for water and its vapor at saturation conditions $\tilde{p}_{sat} = 219 \text{ bar}$ and $\tilde{T}_{sat} = 646.15 \text{ K}$. The superheated temperature of the bottom plate, $\Delta\tilde{T}_{sup} = 10 \text{ K}$ is used similar to numerical studies of 2D film boiling in [23–25,37,38,43,46] and 3D film boiling in [1,41,45]. For the results presented here, the characteristic reference quantities are based on the thermophysical properties of the working fluids [1,38,43]. Based on dimensional analysis [1,38], the capillary length scale is $\tilde{\lambda}_0 = \sqrt{\frac{\sigma}{g(\tilde{\rho}_l - \tilde{\rho}_v)}}$, the time scale $\tilde{t}_0 = \sqrt{\frac{\tilde{\lambda}_0}{g}}$ and the velocity scale $\tilde{U}_0 = \sqrt{\tilde{\lambda}_0 g}$. Rayleigh-Taylor instability (RTI) arises due to the presence of a high-density liquid phase over the low-density vapor phase, whose critical length-scale is expressed in terms of the capillary length as $\tilde{\lambda}_c = 2\pi\tilde{\lambda}_0$. In 2D and 3D film boiling flows, the most dangerous unstable wavelength is related to the critical wavelength, $\tilde{\lambda}_{d2} = \sqrt{3}\tilde{\lambda}_c$ and $\tilde{\lambda}_{d3} = \sqrt{2}\tilde{\lambda}_{d2}$, respectively. The size of the computational domain for film boiling problems is therefore typically based on this most dangerous Taylor wavelength [38,43]. As in [1], the rectangular computational domain we use has size $1 \times 1 \times 2$ in terms of the 3D most dangerous Taylor

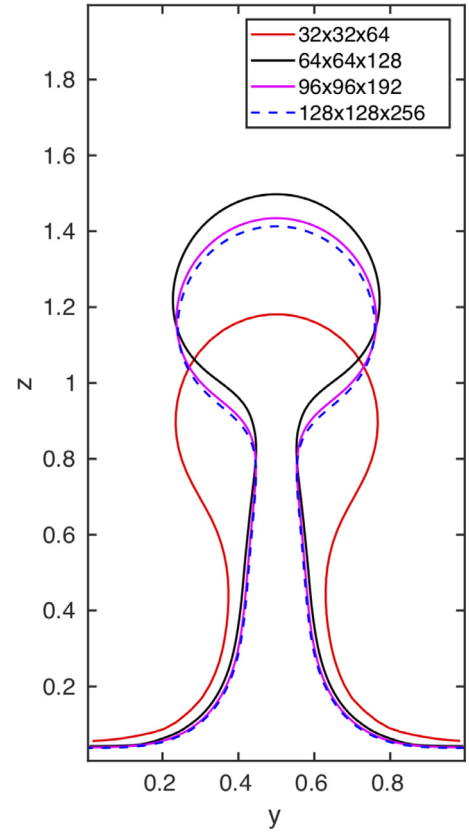


Fig. 8. Interface morphology obtained at non-dimensional time, $t = 34.77$ from the grid sensitivity study of 3D saturated film boiling.

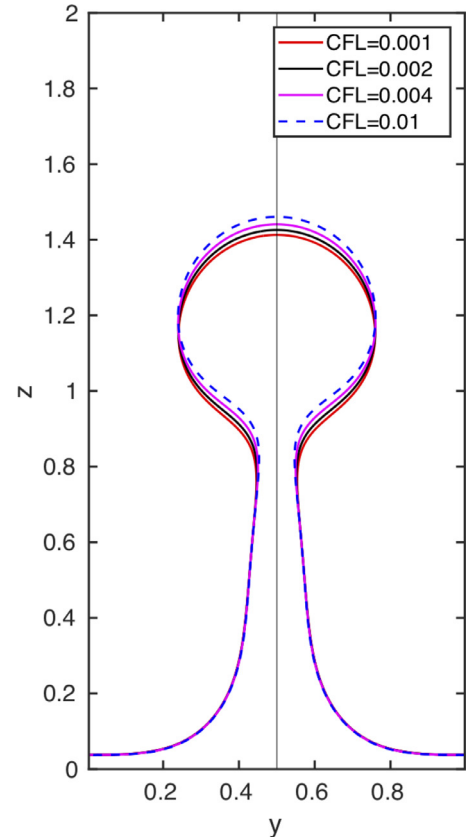


Fig. 9. Interface morphology obtained at non-dimensional time, $t = 34.77$ from the time step convergence study of 3D saturated film boiling.

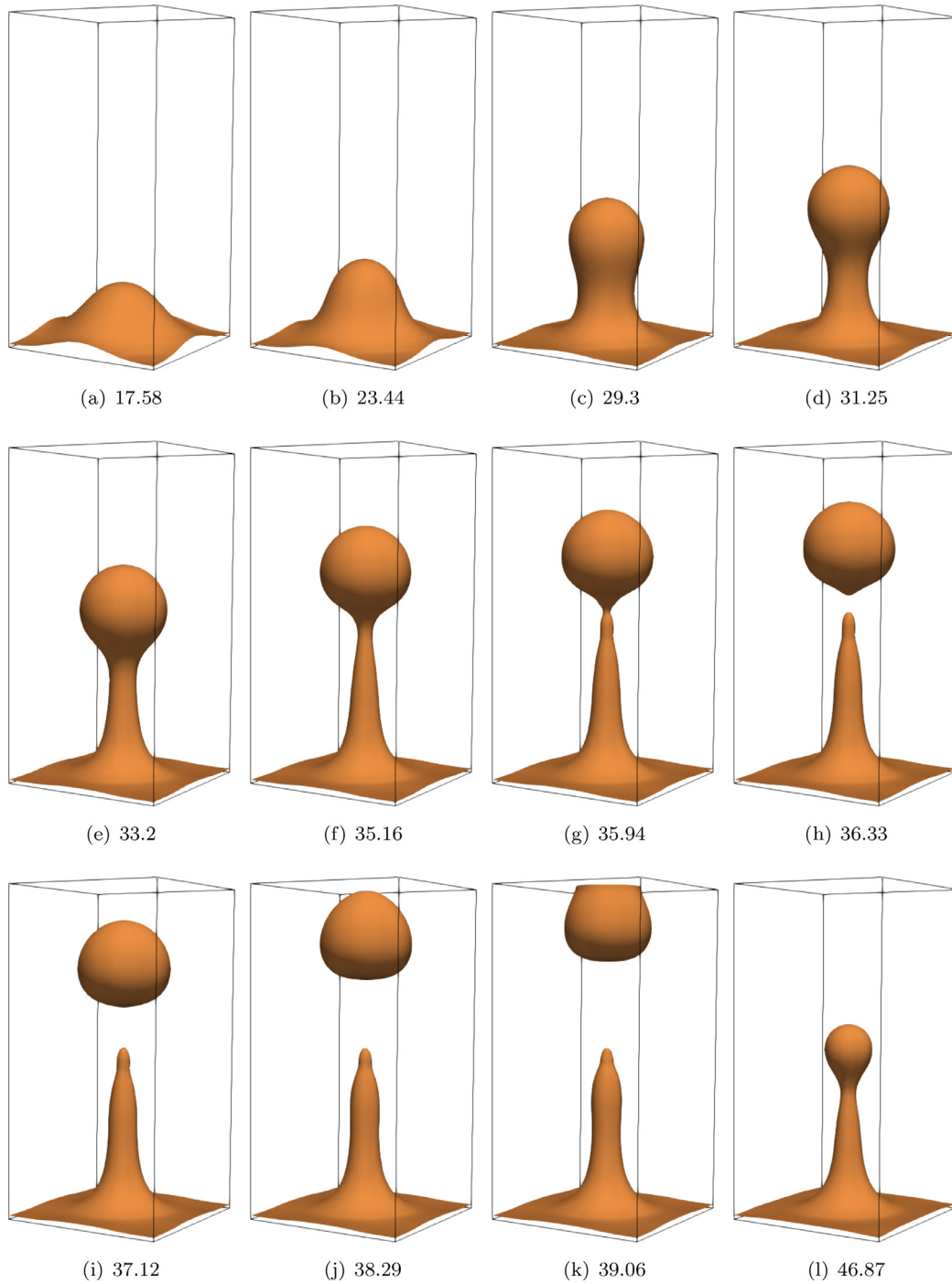


Fig. 10. Transient evolution of the interface morphologies for the 3D film boiling of water and its vapor at $\bar{p}_{sat} = 219 \text{ bar}$ and $\bar{T}_{sat} = 646.15 \text{ K}$ using an uniform wall superheat of $\Delta \bar{T}_{sup} = 10 \text{ K}$, with corresponding Jacob number, $Ja_v = 12.735$.

wavelength, $\tilde{\lambda}_{d3}$. Moreover, initially, the unstable thin vapor layer has a perturbed thickness, $\delta(X, Y)_Z$

$$\delta(X, Y)_Z = \delta_o + a_w \left[\cos \left(\frac{2\pi NX}{L} \right) + \cos \left(\frac{2\pi NY}{W} \right) \right], \quad (42)$$

where, $\delta_o = 0.125L$ is the initial unperturbed vapor film thickness, $a_w = -0.05$ is the perturbation wave amplitude and $N = 1$ is the perturbation wave number. A linear temperature profile is initialised inside the superheated vapor film. The bulk liquid phase is at saturation temperature, $\theta_l = \theta_{sat} = 0$. The perturbed vapor film

thickness, $\delta(X, Y)_Z$ and initial linear temperature profile, θ are displayed in Fig. 7.

For boiling flows, the grid resolution and time step are dependent on the operating conditions of the working fluids [1,23]. In this study, the rectangular domain is discretized using a uniform grid size with $32 \times 32 \times 64$, $64 \times 64 \times 128$, $96 \times 96 \times 192$ and $128 \times 128 \times 256$ cells. The time step, Δt is calculated with a constant CFL number, $c = 0.001$ and uniform wall superheat, $\Delta \bar{T}_{sup} = 10 \text{ K}$. The instantaneous liquid-vapor interface morphology at non-dimensional time, $t = 34.77$ is shown in Fig. 8 for the various grid resolution considered. The interface represented by the

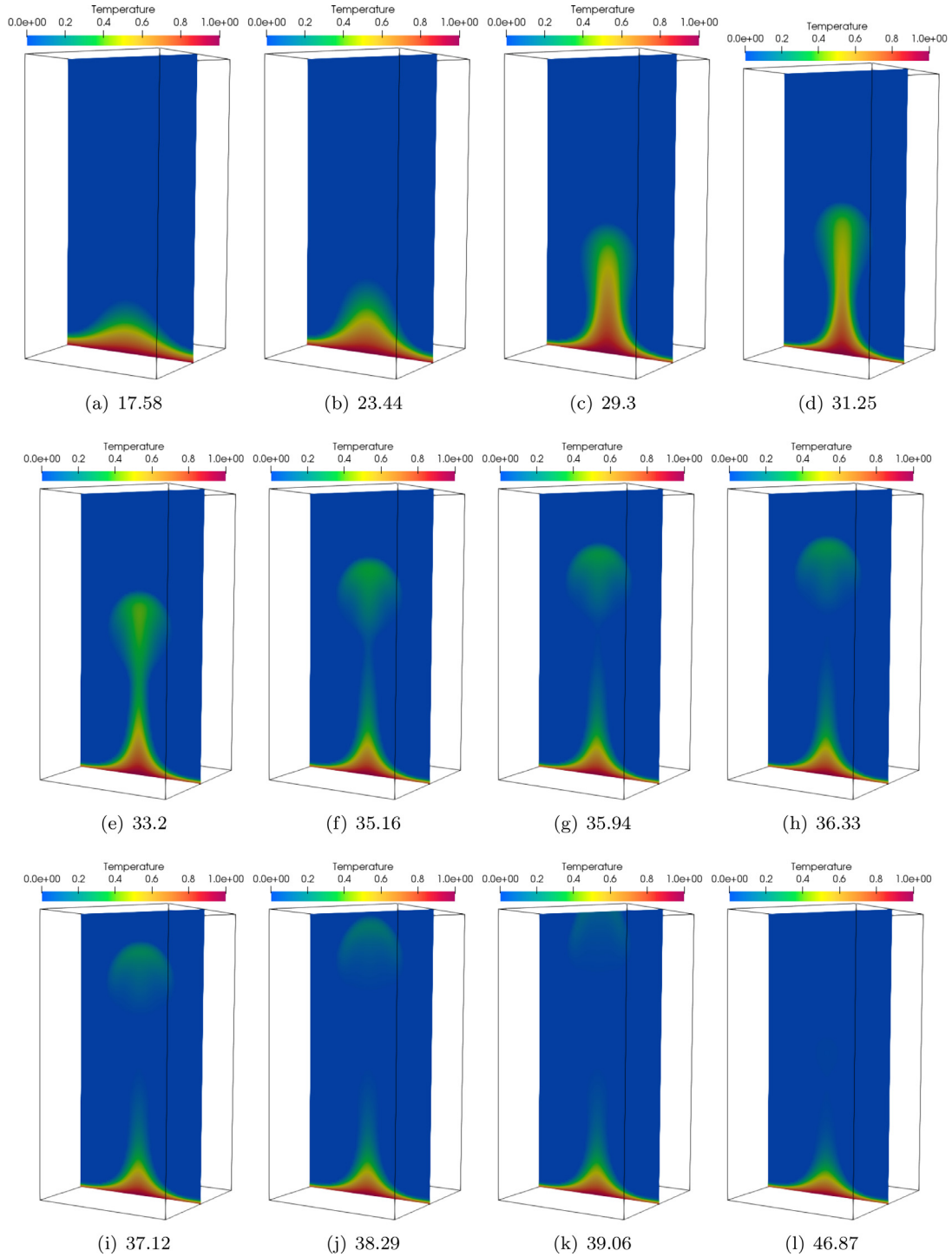


Fig. 11. Transient distribution of the non-dimensional temperature during 3D film boiling of water and its vapor at $\bar{p}_{sat} = 219 \text{ bar}$ and $\bar{T}_{sat} = 646.15 \text{ K}$ using a uniform wall superheat of $\Delta \bar{T}_{sup} = 10 \text{ K}$, corresponding to a Jacob number, $Ja_v = 12.735$.

Heaviside function value $H(\phi) = 0.5$, shows smaller deviations at the two highest grid resolutions considered $96 \times 96 \times 192$ and $128 \times 128 \times 256$. The mesh domain with $128 \times 128 \times 256$ grid cells is therefore adopted for the following simulations.

In computations, the selected time step must satisfy the CFL condition as well as the capillary constraint [46]. We therefore examine the convergence for various CFL numbers, $c = 0.01$, 0.004 , 0.002 and 0.001 for the uniform grid of size $128 \times 128 \times 256$. Fig. 9 displays the bubble interface obtained with the different values of the CFL number. The differences are negligible for CFL num-

bers $c = 0.002$ and $c = 0.001$. For the next simulations, we therefore choose a CFL number equal to 0.001 .

Next, we investigate saturated film boiling of water and its vapor at saturation condition $\bar{p}_{sat} = 219 \text{ bar}$ and $\bar{T}_{sat} = 646.15 \text{ K}$ with a wall superheat, $\Delta \bar{T}_{sup} = 10 \text{ K}$, corresponding to a vapor phase Jacob number, $Ja_v = 12.735$. The transient evolution of the vapour film thickness during the formation of the first bubble is shown in Fig. 10. The thin perturbed vapor layer gradually grows into a large spherical bubble, which detaches and rises upwards due to buoyancy. The formation of a stable vapor column is observed

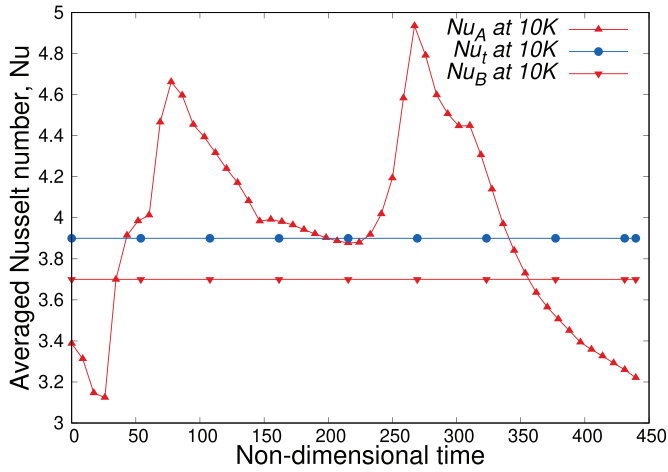


Fig. 12. Space and time averaged Nusselt numbers obtained from 3D film boiling of water and its vapor at wall superheat of 10 K. Nu_B is the prediction from the semi-empirical correlation of Berenson [110,112], whereas the space and time averaged Nu_A and Nu_t are defined in the text.

at $\Delta \tilde{T}_{sup} = 10 K$, with the periodic bubble release cycle occurring at the tip/end of the vapor column. The formation of similar stable vapor columns has been observed in the experimental study [108] and in several 2D numerical studies [24,35,43,46,109]. The non-dimensional temperature distributed at the centre of xz-plane is shown in Fig. 11 for the same test case with time step as in Fig. 10. The temperature distribution inside the vapor phase is superheated whereas the surrounding liquid phase is at the saturation condition. The temperature field displays variations corresponding to the periodic bubble release cycle.

For the heat transfer analysis, we compute the variations of local Nusselt number, $Nu_{x,y}$, a space averaged Nusselt number, Nu_A and the time averaged Nusselt number, Nu_t over the superheated flat surface [24,37] as

$$Nu_{x,y} = \frac{\tilde{\lambda}_o}{\tilde{\lambda}_{d3}} \frac{\partial \theta}{\partial Z}, \quad (43)$$

$$Nu_A = \frac{1}{A} \int_0^A Nu_{x,y} dA, \quad (44)$$

$$Nu_t = \frac{1}{t} \int_0^t Nu_A dt. \quad (45)$$

In laminar film-boiling studies, the semi-empirical correlations of Berenson [110] for Nu_B and Klimenko [111] for Nu_K are usually considered [45],

$$Nu_B = 0.425 \left(\frac{Gr_v Pr_v}{Ja_v} \right)^{\frac{1}{4}}, \quad (46)$$

$$Nu_K = 0.19 (Gr_v Pr_v)^{\frac{1}{3}}. \quad (47)$$

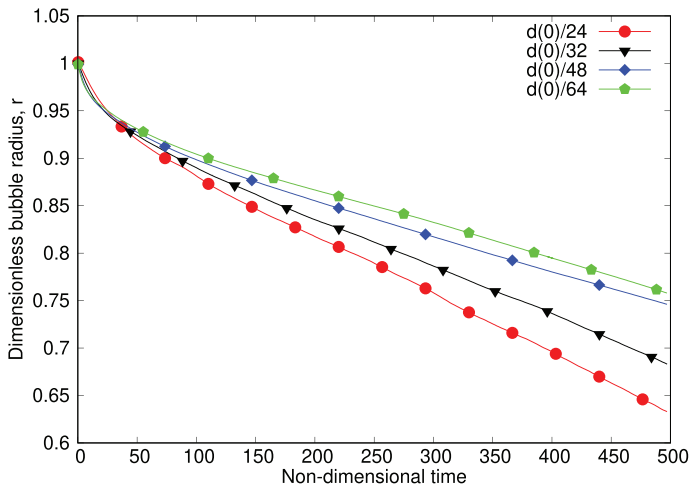
For the conditions of our film boiling simulations, the averaged Nusselt numbers calculated from the correlations of Berenson [110,112], Nu_B and Klimenko [111], Nu_K are 3.696 and 7.935, respectively. The transient variations of the space averaged Nusselt number Nu_A and the time averaged Nusselt number Nu_t obtained from the present 3D film boiling are therefore compared with the semi-empirical correlation of Berenson [110,112] in Fig. 12. This result indicates that the space averaged Nusselt number fluctuates over the horizontal plane superheated surface due to variations in the vapor film thickness, with the peak of the space averaged Nusselt number is corresponding to lower thickness of the vapor film. The time averaged Nusselt number, Nu_t obtained from the MICLS-GFM method is $Nu_t = 3.9$ which slightly deviates from the semi-empirical correlation of Berenson [110,112] by 5.4%.

4.2. Subcooled condensation of a spherical vapor bubble

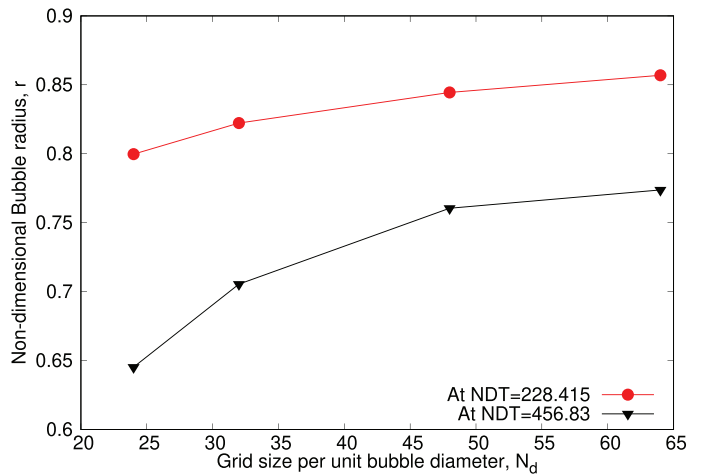
The mass conservative LS method is further used to simulate 3D subcooled pool boiling flow for high density and viscosity ratios. A saturated spherical vapor bubble is placed inside a pool of quiescent subcooled liquid water. The water and its vapor are studied at two different operating conditions of saturated pressure and temperature of $\tilde{p}_{sat} = 1 \text{ bar}$, $\tilde{T}_{sat} = 373 K$ and $\tilde{p}_{sat} = 30 \text{ bar}$, $\tilde{T}_{sat} = 506.7 K$ for three liquid subcooled temperatures, $\Delta \tilde{T}_{sub}$ of 5 K, 12 K and 30 K. The evolution of the condensing bubble volume and its relative or dispersed velocity are examined below.

Following the experimental study of Kim and Park [71] and numerical study of Bahreini et al. [76], we consider a spherical vapor bubble of diameter, $\tilde{D} = 4.7 \text{ mm}$. The bubble size reduces due to the subcooled surrounding liquid.

We examine different grid resolutions, $\Delta h = d(0)/N_d = 1/16$, $1/24$, $1/32$, $1/48$ and $1/64$, while neglecting the acceleration due



(a) Time history of bubble radius



(b) Convergence at fixed time

Fig. 13. Transient evolution of a spherical bubble radius in subcooled boiling at various grids resolution.

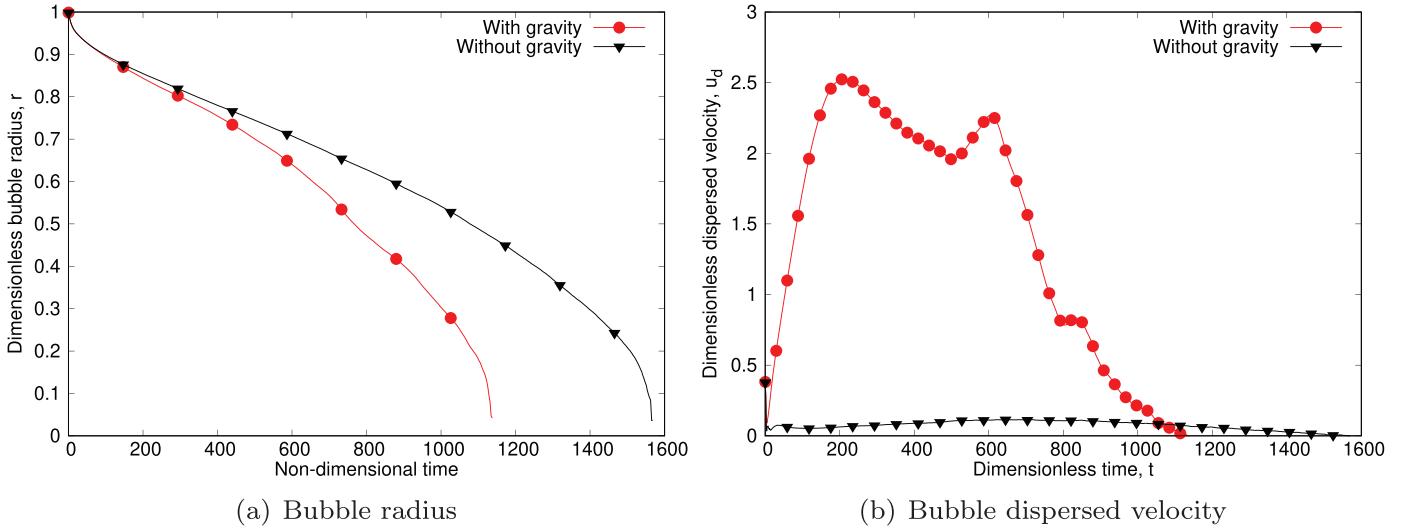


Fig. 14. Subcooled boiling of saturated water at $\bar{p}_{sat} = 1 \text{ atm}$ and $\bar{T}_{sat} = 373 \text{ K}$ with subcooled temperature, $\Delta\bar{T}_{sub} = 30 \text{ K}$ without and with gravity.

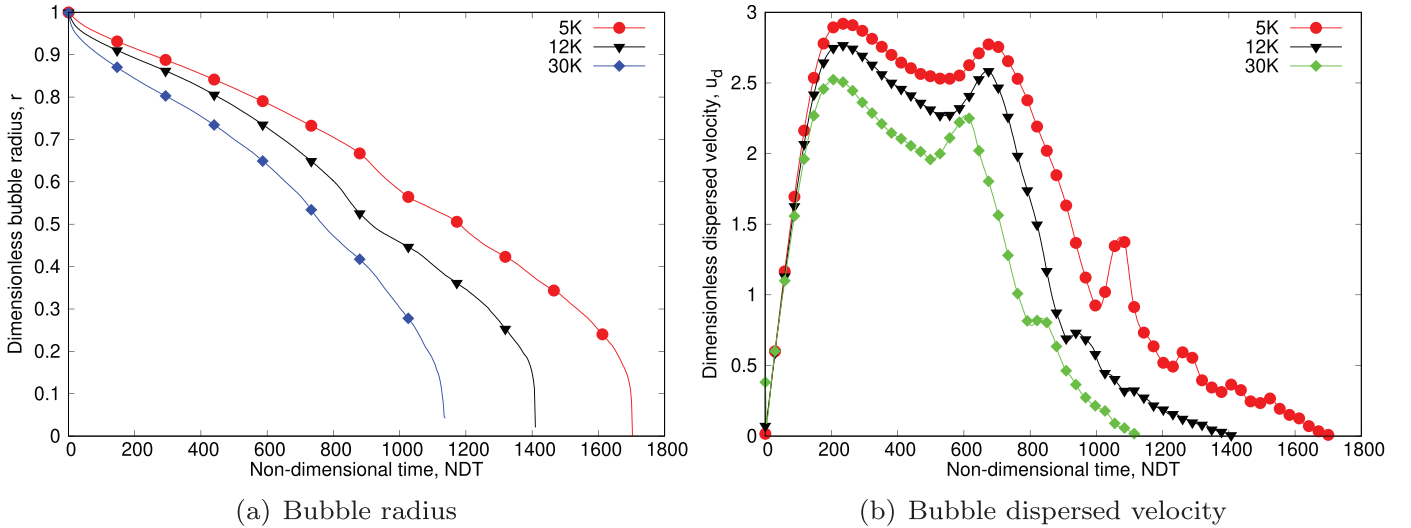


Fig. 15. Subcooled boiling of water at $\bar{p}_{sat} = 1 \text{ atm}$ and $\bar{T}_{sat} = 373 \text{ K}$ at different subcooling temperatures, $\Delta\bar{T}_{sub}$.

to gravity. The time step, Δt is calculated at uniform CFL number, $c = 0.001$. A static spherical bubble is initially placed inside the non-dimensional cubic computational domain of size, $2d(0) \times 2d(0) \times 2d(0)$. The time history of the non-dimensional bubble radius, $r(t)$ obtained at various grid resolutions is shown in Fig. 13(a). From these results it is observed that the condensation of the static bubble is significantly affected by the grid resolution; in particular, the condensation rate is over-predicted by a coarse grid with insufficient resolution. The ratio of surface area to condensing bubble volume, a_b/v_b is higher for a small bubble, leading to very fast condensation when the bubble diameter becomes close to two or three grid sizes, Δh [77]. Therefore, the bubble radius reduces faster when using the coarser grid. The steep gradients of the interface heat and mass flux become inaccurate, which needs to be addressed with adequate grid refinement. Fig. 13(b) shows the variation of the bubble radius at different grid resolutions at fixed dimensionless times, $t = 228.415$ and 456.83 , showing that the results tend to converge at the highest resolutions considered. Thus, to obtain accurate flow and heat transfer data at a reasonable computational cost, the resolution of 48 cells per bubble diameter is used for the simulations of subcooled boiling flow.

The effect of the buoyancy-driven rising motion and condensation of bubbles inside a quiescent subcooled liquid is important for

the cooling of condensers, boilers and nuclear reactors [113]. We therefore examine the potentiality of our method for the case of subcooled pool boiling of buoyancy-driven upward rising bubbles in water at saturation conditions $\bar{p}_{sat} = 1 \text{ atm}$ and $\bar{T}_{sat} = 373 \text{ K}$ with subcooled temperature, $\Delta\bar{T}_{sub} = 30 \text{ K}$. The time history of the condensing bubble radius, $r(t)$ and the corresponding non-dimensional dispersed bubble velocity, u_d are shown in Fig. 14(a) and (b) for a case without and with gravity. As expected, the data show that the condensation of the bubble is faster in the presence of gravity, as is the magnitude of the dispersed velocity. Owing to the buoyancy-driven motion, the bubble undergoes larger deformations, which also further enhance the condensation, as clearly observed in Fig. 14(a).

Next, we consider the effect of temperature and simulate a system of saturated water and its vapor at $\bar{p}_{sat} = 1 \text{ atm}$ and $\bar{T}_{sat} = 373 \text{ K}$, for the subcooled temperatures, $\Delta\bar{T}_{sub}$ of 5 K, 12 K and 30 K, as shown in Fig. 15. A high pressure case, with saturation conditions $\bar{p}_{sat} = 30 \text{ atm}$, and $\bar{T}_{sat} = 508.15 \text{ K}$ at various subcooled temperatures, $\Delta\bar{T}_{sub}$ of 5 K, 12 K and 30 K, is shown in Fig. 16(a) and (b). The condensation rate of the spherical bubble increases with increasing subcooling of the bulk liquid. The bubble dispersed velocity magnitude decreases when increasing the subcooling of the water. Due to the change in thermophysical properties of water

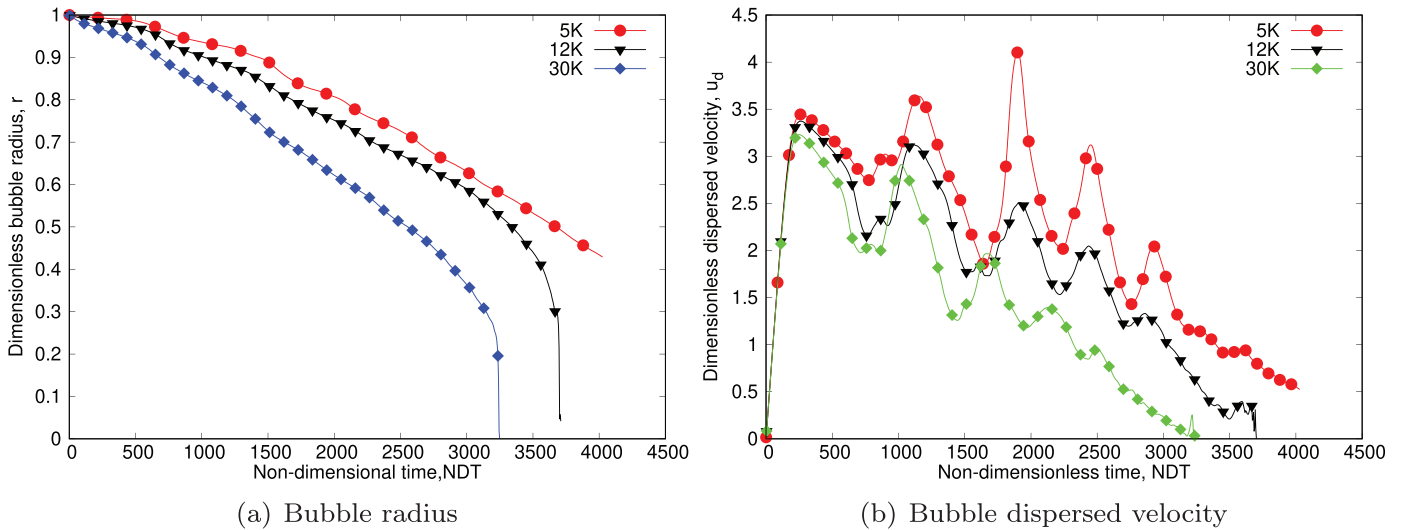


Fig. 16. Subcooled boiling of water at $\bar{p}_{sat} = 30 \text{ atm}$ and $\bar{T}_{sat} = 508.15 \text{ K}$ at different subcooling temperatures, $\Delta \bar{T}_{sub}$.

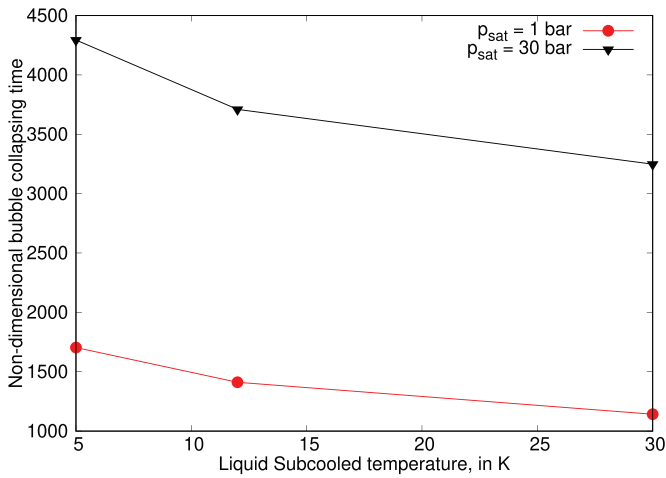


Fig. 17. The spherical bubble collapsing time at various liquid subcooled temperatures for 3D subcooled boiling of water and its vapor at various pressure conditions, \bar{p}_{sat} of 1 bar and 30 bar.

at different saturation conditions, the condensation rate decreases when increasing the saturation pressure.

Finally, we compare the dimensionless bubble collapsing time at different liquid subcooling temperatures and for different saturation pressures in Fig. 17. The non-dimensional bubble collapsing time for the saturation condition $\bar{p}_{sat} = 30 \text{ bar}$ is higher than at $\bar{p}_{sat} = 1 \text{ bar}$ as already noted. It is also observed that at fixed saturation conditions, the non-dimensional bubble collapsing time decreases when increasing the liquid subcooling, $\Delta \bar{T}_{sub}$.

5. Conclusions

In this numerical study, we present a mass-conserving interface-correction level-set (MICLS) algorithm, based on the ghost-fluid method (GFM), to perform direct numerical simulations of three-dimensional boiling flows. For the velocity-pressure coupling, a staggered grid based projection method with fast pressure Poisson solver is employed. The interface jump conditions due to phase change are modeled by a second-order accurate linear ghost extrapolation approach. The divergence condition at the interface (non-zero for phase change) and corresponding normal velocity is computed using a simple ghost-velocity extension approach. The

present GFM-based phase-change model is extensively evaluated based on both qualitative and quantitative analyses. Validations of the advection algorithm and linear extrapolation for ghost velocity extension, ghost temperature and ghost interface mass flux across the interface are considered, and different phase-change benchmark cases are presented. The overall results are summarized below.

1. To evaluate the modified LS advection, re-distancing and curvature-dependent mass correction for phase change problems we consider the expansion of a spherical bubble at uniform rate. We compare the evolution of the dimensionless bubble diameter and absolute error or L_1 error norms obtained using a classical LS method, the MICLS with exact reference volume and the MICLS with modified reference volume with the analytical solution, reporting close agreement with the analytical solution. The modified MICLS accurately captures the bubble dynamics even under coarse grid resolutions, thus offering lower computational costs than the classical LS method.
2. We validate the MICLS with the projection method for velocity-pressure coupling, with GFM surface tension and the ghost velocity extension across the interface for the test case of uniform phase change. On each cell, a momentum equation for the fluid velocity and ghost fluid velocity components are independently solved with a continuous jump condition. Comparing with the analytical solution, we conclude that a minimum dimensionless grid size of 32 cells per unit diameter is necessary to correctly capture the interface morphology and flow physics.
3. To validate the computation of the non-uniform interface normal velocity due to heat and mass fluxes across the interface, a one-dimensional Stefan problem is considered, for which an analytical solution exists. Comparisons are presented for the non-dimensional plane interface thickness and interface non-uniform velocity.
4. To further validate the MICLS-GFM method for 3D boiling flows, we present results for 3D single-mode saturated film boiling of water at near-critical conditions of saturated pressure, $\bar{p}_{sat} = 219 \text{ bar}$ and saturated temperature, $\bar{T}_{sat} = 646.15 \text{ K}$ over a horizontal plane superheated surface at wall superheating of $\Delta \bar{T}_{sup} = 10 \text{ K}$, with corresponding vapor Jacob number, $Ja_v = 12.375$. The dimensionless interface unstable film thickness, non-dimensional temperature distribution, space-averaged Nusselt number and time-averaged wall Nusselt number show trends similar to 2D and 3D film boiling studies in the liter-

ature. The time averaged Nusselt number obtained with the present MICLS-GFM method is found to deviate by 5.4% with respect to the value from the semi-empirical correlation of Berenson [110,112].

5. To evaluate the present MICLS-GFM model for cases with high density and viscosity ratios, we consider water and its vapor at saturation conditions of $\tilde{p}_{sat} = 1 \text{ bar}$ and $\tilde{p}_{sat} = 30 \text{ bar}$. We therefore simulate 3D condensation of a saturated spherical water vapor bubble placed inside a pool of subcooled liquid water. The rate of bubble condensation is evaluated with and without gravity effect at different subcooling temperatures. The time history of the bubble dynamics is computed based on the non-dimensional bubble shrinking diameter. We observe that:

- the subcooled boiling shows lower rate of bubble condensation and lower magnitudes of bubble dispersed velocity in the absence of gravity, due to the absence of buoyancy effects.
- the increase of liquid subcooling increases the bubble condensation rate due to higher mass flux, and leads to faster bubble collapsing with lower magnitudes of dispersed bubble velocity.
- The interface mass flux is depends on the thermophysical properties and latent heat of the working fluids. The ratio of thermophysical properties and latent heat of vaporization of the water and its vapor at saturation condition of $\tilde{p}_{sat} = 1 \text{ bar}$ is higher as compared to saturation condition of $\tilde{p}_{sat} = 30 \text{ bar}$. Hence, the bubble condensation rate is higher for the water at saturation condition of $\tilde{p}_{sat} = 1 \text{ bar}$. However, the magnitudes of the condensing bubble dimensionless dispersed velocity is lower for water and its vapor at saturation condition of $\tilde{p}_{sat} = 1 \text{ bar}$.
- Finally, the non-dimensional bubble collapsing time for the saturation condition of $\tilde{p}_{sat} = 30 \text{ bar}$ is higher due to the lower rate of bubble condensation. At fixed saturation conditions, the non-dimensional bubble collapsing time decreases by increasing in the liquid subcooling, $\Delta \tilde{T}_{sub}$.

Declaration of Competing Interest

This article has not been presented to any other journals and not published anywhere else. I acknowledge that I have no conflict of interest.

Acknowledgements

This research is supported by the Linné Flow Centre at KTH Mechanics, Stockholm, Sweden. The computing time is provided by SNIC (Swedish National Infrastructure for Computing), in particular resources at PDC in Stockholm. We thank Dr. Daulet Izbassarov, postdoc at KTH Mechanics, for his HPC support.

Supplementary material

Supplementary material associated with this article can be found, in the online version, at [10.1016/j.ijheatmasstransfer.2020.120382](https://doi.org/10.1016/j.ijheatmasstransfer.2020.120382).

References

- [1] A. Esmaeili, G. Tryggvason, Computations of film boiling. Part i: numerical method, *Int. J. Heat Mass Transf.* 47 (25) (2004) 5451–5461.
- [2] M. Chamoun, R. Rulliere, P. Haberschill, J.-L. Peureux, Experimental and numerical investigations of a new high temperature heat pump for industrial heat recovery using water as refrigerant, *Int. J. Refrig.* 44 (2014) 177–188.
- [3] J. Lee, Y. Kim, S. Jeong, Transient thermodynamic behavior of cryogenic mixed fluid thermosiphon and its cool-down time estimation, *Cryogenics* 50 (5) (2010) 352–358.
- [4] M. Gravlee, C. Vera, M. Wollen, C. McLean, L. Walls, Micro-gravity cryogenic experiment opportunity, in: *AIAA SPACE 2010 Conference & Exposition*, 2010, p. 8838.
- [5] P. Sabharwall, V. Utgikar, A. Tokuhiko, F. Gunnerson, Design of liquid metal phase change heat exchanger for next-generation nuclear plant process heat application, *J. Nucl. Sci. Technol.* 46 (6) (2009) 534–544.
- [6] Y. Wang, Z.-g. Wang, An overview of liquid-vapor phase change, flow and heat transfer in mini-and micro-channels, *Int. J. Therm. Sci.* 86 (2014) 227–245.
- [7] A. Prosperetti, G. Tryggvason, *Computational Methods for Multiphase Flow*, Cambridge University Press, 2009.
- [8] Y. Li, J. Zhang, L.-S. Fan, Discrete-phase simulation of single bubble rise behavior at elevated pressures in a bubble column, *Chem. Eng. Sci.* 55 (20) (2000) 4597–4609.
- [9] D. Pfleger, S. Gomes, N. Gilbert, H.-G. Wagner, Hydrodynamic simulations of laboratory scale bubble columns fundamental studies of the Eulerian–Eulerian modelling approach, *Chem. Eng. Sci.* 54 (21) (1999) 5091–5099.
- [10] Y. Zhao, H.H. Tan, B. Zhang, A high-resolution characteristics-based implicit dual time-stepping VOF method for free surface flow simulation on unstructured grids, *J. Comput. Phys.* 183 (1) (2002) 233–273.
- [11] H. Deconinck, C. Hirsch, A multigrid method for the transonic full potential equation discretized with finite elements on an arbitrary body fitted mesh, *J. Comput. Phys.* 48 (3) (1982) 344–365.
- [12] S.W. Welch, Local simulation of two-phase flows including interface tracking with mass transfer, *J. Comput. Phys.* 121 (1) (1995) 142–154.
- [13] S.O. Unverdi, G. Tryggvason, A front-tracking method for viscous, incompressible, multi-fluid flows, *J. Comput. Phys.* 100 (1) (1992) 25–37.
- [14] R. Chen, W. Tian, G. Su, S. Qiu, Y. Ishiwatari, Y. Oka, Numerical investigation on bubble dynamics during flow boiling using moving particle semi-implicit method, *Nucl. Eng. Des.* 240 (11) (2010) 3830–3840.
- [15] W. Tian, Y. Ishiwatari, S. Ikejiri, M. Yamakawa, Y. Oka, Numerical computation of thermally controlled steam bubble condensation using moving particle semi-implicit (MPS) method, *Ann. Nucl. Energy* 37 (1) (2010) 5–15.
- [16] S. Koshizuka, Y. Oka, Moving-particle semi-implicit method for fragmentation of incompressible fluid, *Nucl. Sci. Eng.* 123 (3) (1996) 421–434.
- [17] S. Osher, J.A. Sethian, Fronts propagating with curvature-dependent speed: algorithms based on Hamilton-Jacobi formulations, *J. Comput. Phys.* 79 (1) (1988) 12–49.
- [18] O. Desjardins, V. Moureau, H. Pitsch, An accurate conservative level set/ghost fluid method for simulating turbulent atomization, *J. Comput. Phys.* 227 (18) (2008) 8395–8416.
- [19] W.J. Rider, D.B. Kothe, Reconstructing volume tracking, *J. Comput. Phys.* 141 (2) (1998) 112–152.
- [20] J. López, J. Hernández, P. Gómez, F. Faura, A volume of fluid method based on multidimensional advection and spline interface reconstruction, *J. Comput. Phys.* 195 (2) (2004) 718–742.
- [21] J. López, J. Hernández, Analytical and geometrical tools for 3d volume of fluid methods in general grids, *J. Comput. Phys.* 227 (12) (2008) 5939–5948.
- [22] M. Sussman, E.G. Puckett, A coupled level set and volume-of-fluid method for computing 3d and axisymmetric incompressible two-phase flows, *J. Comput. Phys.* 162 (2) (2000) 301–337.
- [23] B. Ninge Gowda, B. Premachandran, A coupled level set and volume of fluid method with multi-directional advection algorithms for two-phase flows with and without phase change, *Int. J. Heat Mass Transf.* 79 (2014) 532–550.
- [24] B. Ninge Gowda, B. Premachandran, Numerical investigation of the pool film boiling of water and R134a over a horizontal surface at near-critical conditions, *Numer. Heat Transf. Part A Appl.* (2017) 1–28.
- [25] B. Ninge Gowda, B. Premachandran, Saturated film boiling of water over a finite size heater, *Int. J. Therm. Sci.* 135 (2019) 417–433.
- [26] B. Ninge Gowda, B. Premachandran, Free convection film boiling over a discrete flat heater with different surface orientations, *Numer. Heat Transf. Part A Appl.* 76 (9) (2019) 712–723.
- [27] D. Sun, W. Tao, A coupled volume-of-fluid and level set (VOSET) method for computing incompressible two-phase flows, *Int. J. Heat Mass Transf.* 53 (4) (2010) 645–655.
- [28] H. Zheng, C. Shu, Y.-T. Chew, A lattice Boltzmann model for multiphase flows with large density ratio, *J. Comput. Phys.* 218 (1) (2006) 353–371.
- [29] J. Brackbill, D.B. Kothe, C. Zemach, A continuum method for modeling surface tension, *J. Comput. Phys.* 100 (2) (1992) 335–354.
- [30] D. Gueyffier, J. Li, A. Nadim, R. Scardovelli, S. Zaleski, Volume-of-fluid interface tracking with smoothed surface stress methods for three-dimensional flows, *J. Comput. Phys.* 152 (2) (1999) 423–456.
- [31] Y. Renardy, M. Renardy, PROST: A parabolic reconstruction of surface tension for the volume-of-fluid method, *J. Comput. Phys.* 183 (2) (2002) 400–421.
- [32] R.P. Fedkiw, T. Aslam, B. Merriman, S. Osher, A non-oscillatory Eulerian approach to interfaces in multimaterial flows (the ghost fluid method), *J. Comput. Phys.* 152 (2) (1999) 457–492.
- [33] S. Tanguy, M. Sagan, B. Lalanne, F. Couderc, C. Colin, Benchmarks and numerical methods for the simulation of boiling flows, *J. Comput. Phys.* 264 (2014) 1–22.
- [34] S. Popinet, Numerical models of surface tension, *Annu. Rev. Fluid Mech.* 50 (1) (2018) 49–75, doi:10.1146/annurev-fluid-122316-045034.
- [35] F. Gibou, L. Chen, D. Nguyen, S. Banerjee, A level set based sharp interface method for the multiphase incompressible Navier-Stokes equations with phase change, *J. Comput. Phys.* 222 (2) (2007) 536–555.

- [36] D. Juric, G. Tryggvason, Computations of boiling flows, *Int. J. Multiphase Flow* 24 (3) (1998) 387–410.
- [37] G. Son, V.K. Dhir, Numerical simulation of film boiling near critical pressures with a level set method, *J. Heat Transf.* 120 (1) (1998) 183–192.
- [38] S.W. Welch, J. Wilson, A volume of fluid based method for fluid flows with phase change, *J. Comput. Phys.* 160 (2) (2000) 662–682.
- [39] S. Tanguy, T. Ménard, A. Berlemont, A level set method for vaporizing two-phase flows, *J. Comput. Phys.* 221 (2) (2007) 837–853.
- [40] C.R. Kharangate, I. Mudawar, Review of computational studies on boiling and condensation, *Int. J. Heat Mass Transf.* 108 (2017) 1164–1196.
- [41] A. Esmaeili, G. Tryggvason, Computations of film boiling. Part ii: multi-mode film boiling, *Int. J. Heat Mass Transf.* 47 (25) (2004) 5463–5476.
- [42] S.W. Welch, T. Rachidi, Numerical computation of film boiling including conjugate heat transfer, *Numer. Heat Transf. Part B Fundam.* 42 (1) (2002) 35–53.
- [43] D. Agarwal, S. Welch, G. Biswas, F. Durst, Planar simulation of bubble growth in film boiling in near-critical water using a variant of the VOF method, *J. Heat Transf.* 126 (3) (2004) 329–338.
- [44] Y.-Y. Tsui, S.-W. Lin, Y.-N. Lai, F.-C. Wu, Phase change calculations for film boiling flows, *Int. J. Heat Mass Transf.* 70 (2014) 745–757.
- [45] Y.-Y. Tsui, S.-W. Lin, Three-dimensional modeling of fluid dynamics and heat transfer for two-fluid or phase change flows, *Int. J. Heat Mass Transf.* 93 (2016) 337–348.
- [46] G. Tomar, G. Biswas, A. Sharma, A. Agrawal, Numerical simulation of bubble growth in film boiling using a coupled level-set and volume-of-fluid method, *Phys. Fluids* 17 (11) (2005) 112103.
- [47] B. Níngegowda, B. Premachandran, Numerical simulation of two-dimensional forced convective film boiling flow over a horizontal flat surface, *Procedia IUTAM* 15 (2015) 256–263.
- [48] N.K. Singh, B. Premachandran, A coupled level set and volume of fluid method on unstructured grids for the direct numerical simulations of two-phase flows including phase change, *Int. J. Heat Mass Transf.* 122 (2018) 182–203.
- [49] D. Guo, D. Sun, Z. Li, W. Tao, Phase change heat transfer simulation for boiling bubbles arising from a vapor film by the VOSET method, *Numer. Heat Transf. Part A Appl.* 59 (11) (2011) 857–881.
- [50] K. Ling, Z.-H. Li, D.-L. Sun, Y.-L. He, W.-Q. Tao, A three-dimensional volume of fluid & level set (VOSET) method for incompressible two-phase flow, *Comput. Fluids* 118 (2015) 293–304.
- [51] Z. Cao, D. Sun, B. Yu, J. Wei, A coupled volume-of-fluid and level set (VOSET) method based on remapping algorithm for unstructured triangular grids, *Int. J. Heat Mass Transf.* 111 (2017) 232–245.
- [52] Z. Cao, D. Sun, J. Wei, B. Yu, A coupled volume-of-fluid and level set method based on multi-dimensional advection for unstructured triangular meshes, *Chem. Eng. Sci.* 176 (2018) 560–579.
- [53] S. Gong, P. Cheng, Lattice Boltzmann simulation of periodic bubble nucleation, growth and departure from a heated surface in pool boiling, *Int. J. Heat Mass Transf.* 64 (2013) 122–132.
- [54] Q. Li, Q. Kang, M.M. Francois, Y. He, K. Luo, Lattice Boltzmann modeling of boiling heat transfer: the boiling curve and the effects of wettability, *Int. J. Heat Mass Transf.* 85 (2015) 787–796.
- [55] L.R. Villegas, R. Alis, M. Lepilliez, S. Tanguy, A ghost fluid/level set method for boiling flows and liquid evaporation: application to the leidenfrost effect, *J. Comput. Phys.* 316 (2016) 789–813.
- [56] L.R. Villegas, S. Tanguy, G. Castanet, O. Caballina, F. Lemoine, Direct numerical simulation of the impact of a droplet onto a hot surface above the leidenfrost temperature, *Int. J. Heat Mass Transf.* 104 (2017) 1090–1109.
- [57] G. Huber, S. Tanguy, M. Sagan, C. Colin, Direct numerical simulation of nucleate pool boiling at large microscopic contact angle and moderate Jakob number, *Int. J. Heat Mass Transf.* 113 (2017) 662–682.
- [58] A. Urbano, S. Tanguy, G. Huber, C. Colin, Direct numerical simulation of nucleate boiling in micro-layer regime, *Int. J. Heat Mass Transf.* 123 (2018) 1128–1137.
- [59] A. Orazzo, S. Tanguy, Direct numerical simulations of droplet condensation, *Int. J. Heat Mass Transf.* 129 (2019) 432–448.
- [60] E.-R. Popescu, S. Tanguy, C. Colin, On the influence of liquid/vapor phase change onto the Nusselt number of a laminar superheated or subcooled vapor flow, *Int. J. Therm. Sci.* 140 (2019) 397–412.
- [61] N. Scapin, P. Costa, L. Brandt, A volume-of-fluid method for interface-resolved simulations of phase-changing two-fluid flows, *J. Comput. Phys.* 407 (2020) 109251.
- [62] G. Lupo, M.N. Ardekani, L. Brandt, C. Duwig, An immersed boundary method for flows with evaporating droplets, *Int. J. Heat Mass Transf.* 143 (2019) 118563.
- [63] M.S. Lee, A. Riaz, V. Aute, Direct numerical simulation of incompressible multiphase flow with phase change, *J. Comput. Phys.* 344 (2017) 381–418.
- [64] E.J. Owwoye, D. Schubring, Numerical simulation of vapor bubble condensation in turbulent subcooled flow boiling, *Nucl. Eng. Des.* 289 (2015) 126–143.
- [65] E. Krepper, R. Rzehak, C. Lifante, T. Frank, CFD for subcooled flow boiling: Coupling wall boiling and population balance models, *Nucl. Eng. Des.* 255 (2013) 330–346.
- [66] S. Kamei, M. Hirata, Condensing phenomena of a single vapor bubble into subcooled water, *Exp. Heat Transf. Int. J.* 3 (2) (1990) 173–182.
- [67] S. Kamei, M. Hirata, Study on condensation of a single vapor bubble into subcooled water-part 2; experimental analysis, *Heat Transfer-Japanese Research; (USA)*, 19, 1990.
- [68] Y. Chen, F. Mayinger, Measurement of heat transfer at the phase interface of condensing bubbles, *Int. J. Multiphase Flow* 18 (6) (1992) 877–890.
- [69] H. Kalman, Y. Mori, Experimental analysis of a single vapor bubble condensing in subcooled liquid, *Chem. Eng. J.* 85 (2-3) (2002) 197–206.
- [70] D. Lucas, H.-M. Prasser, Steam bubble condensation in sub-cooled water in case of co-current vertical pipe flow, *Nucl. Eng. Des.* 237 (5) (2007) 497–508.
- [71] S.-J. Kim, G.-C. Park, Interfacial heat transfer of condensing bubble in subcooled boiling flow at low pressure, *Int. J. Heat Mass Transf.* 54 (13–14) (2011) 2962–2974.
- [72] D. Lucas, M. Beyer, L. Szalinski, Experimental investigations on the condensation of steam bubbles injected into subcooled water at 1 MPA, *Multiphase Sci. Technol.* 22 (1) (2010).
- [73] S. Al Issa, P. Weisensee, R. Macián-Juan, Experimental investigation of steam bubble condensation in vertical large diameter geometry under atmospheric pressure and different flow conditions, *Int. J. Heat Mass Transf.* 70 (2014) 918–929.
- [74] X.-h. Qu, M.-c. Tian, G.-m. Zhang, X.-l. Leng, Experimental and numerical investigations on the air–steam mixture bubble condensation characteristics in stagnant cool water, *Nucl. Eng. Des.* 285 (2015) 188–196.
- [75] T.T. Nguyen, N. Tsuzuki, H. Murakawa, N.H. Duong, H. Kikura, Measurement of the condensation rate of vapor bubbles rising upward in subcooled water by using two ultrasonic frequencies, *Int. J. Heat Mass Transf.* 99 (2016) 159–169.
- [76] M. Bahreini, A. Ramiar, A.A. Ranjbar, Numerical simulation of bubble behavior in subcooled flow boiling under velocity and temperature gradient, *Nucl. Eng. Des.* 293 (2015) 238–248.
- [77] N. Samkhaniani, M. Ansari, Numerical simulation of bubble condensation using CF-VOF, *Prog. Nucl. Energy* 89 (2016) 120–131.
- [78] S.-S. Jeon, S.-J. Kim, G.-C. Park, Numerical study of condensing bubble in subcooled boiling flow using volume of fluid model, *Chem. Eng. Sci.* 66 (23) (2011) 5899–5909.
- [79] L.-m. Pan, Z.-w. Tan, D.-q. Chen, L.-c. Xue, Numerical investigation of vapor bubble condensation characteristics of subcooled flow boiling in vertical rectangular channel, *Nucl. Eng. Des.* 248 (2012) 126–136.
- [80] Z. Liu, B. Sundén, H. Wu, Numerical modeling of multiple bubbles condensation in subcooled flow boiling, *J. Therm. Sci. Eng. Appl.* 7 (3) (2015) 031003.
- [81] J.-h. Wei, L.-m. Pan, D.-q. Chen, H. Zhang, J.-j. Xu, Y.-p. Huang, Numerical simulation of bubble behaviors in subcooled flow boiling under swing motion, *Nucl. Eng. Des.* 241 (8) (2011) 2898–2908.
- [82] G. Son, V.K. Dhir, A level set method for analysis of film boiling on an immersed solid surface, *Numer. Heat Transf. Part B Fundam.* 52 (2) (2007) 153–177.
- [83] Z. Liu, B. Sundén, J. Yuan, Numerical modelling of condensation of multiple bubbles in subcooled flow boiling with VOF method, in: *ASME 2013 Heat Transfer Summer Conference* collocated with the ASME 2013 7th International Conference on Energy Sustainability and the ASME 2013 11th International Conference on Fuel Cell Science, Engineering and Technology, American Society of Mechanical Engineers, 2013, pages V001T03A014–V001T03A014.
- [84] M.R. Sheykhi, M. Afrand, D. Toghraie, P. Talebizadehsardari, Numerical simulation of critical heat flux in forced boiling of a flow in an inclined tube with different angles, *J. Therm. Anal. Calorim.* 139 (4) (2020) 2859–2880.
- [85] D. Toghraie, Numerical thermal analysis of water's boiling heat transfer based on a turbulent jet impingement on heated surface, *Physica E* 84 (2016) 454–465.
- [86] R. Azadbakhti, F. Pourfattah, A. Ahmadi, O.A. Akbari, D. Toghraie, Eulerian–Eulerian multi-phase RPI modeling of turbulent forced convective of boiling flow inside the tube with porous medium, *Int. J. Numer. Methods Heat Fluid Flow* (2019).
- [87] D.T. Semiromi, A. Azimian, Molecular dynamics simulation of annular flow boiling with the modified Lennard-Jones potential function, *Heat Mass Transf.* 48 (1) (2012) 141–152.
- [88] M. Zarringhalam, H. Ahmadi-Danesh-Ashtiani, D. Toghraie, R. Fazaeli, The effects of suspending copper nanoparticles into argon base fluid inside a microchannel under boiling flow condition by using of molecular dynamic simulation, *J. Mol. Liquids* 293 (2019) 111474.
- [89] M. Zarringhalam, H. Ahmadi-Danesh-Ashtiani, D. Toghraie, R. Fazaeli, Molecular dynamic simulation to study the effects of roughness elements with cone geometry on the boiling flow inside a microchannel, *Int. J. Heat Mass Transf.* 141 (2019) 1–8.
- [90] Y. Peng, M. Zarringhalam, M. Hajian, D. Toghraie, S.J. Tadi, M. Afrand, Empowering the boiling condition of argon flow inside a rectangular microchannel with suspending silver nanoparticles by using of molecular dynamics simulation, *J. Mol. Liq.* 295 (2019) 111721.
- [91] Y. Peng, M. Zarringhalam, A.A. Barzinjy, D. Toghraie, M. Afrand, Effects of surface roughness with the spherical shape on the fluid flow of argon atoms flowing into the microchannel, under boiling condition using molecular dynamic simulation, *J. Mol. Liq.* 297 (2020) 111650.
- [92] S. Rostami, H. Ahmadi-Danesh-Ashtiani, D. Toghraie, R. Fazaeli, A statistical method for simulation of boiling flow inside a platinum microchannel, *Physica A* (2019) 123879.
- [93] S.-R. Yan, N. Shirani, M. Zarringhalam, D. Toghraie, Q. Nguyen, A. Karimipour, Prediction the boiling flow characteristics in rough and smooth microchannels using of molecular dynamics simulation: investigation the effects of boundary wall temperatures, *J. Mol. Liq.* (2020) 112937.
- [94] Z. Ge, J.-C. Loiseau, O. Tammisola, L. Brandt, An efficient mass-preserving interface-correction level set/ghost fluid method for droplet suspensions under depletion forces, *J. Comput. Phys.* 353 (2018) 435–459.
- [95] M.S. Dodd, A. Ferrante, A fast pressure-correction method for incompressible two-fluid flows, *J. Comput. Phys.* 273 (2014) 416–434.

- [96] T.D. Aslam, A partial differential equation approach to multidimensional extrapolation, *J. Comput. Phys.* 193 (1) (2004) 349–355.
- [97] C. Shao, K. Luo, M. Chai, H. Wang, J. Fan, A computational framework for interface-resolved DNS of simultaneous atomization, evaporation and combustion, *J. Comput. Phys.* 371 (2018) 751–778.
- [98] F. Gibou, R.P. Fedkiw, L.-T. Cheng, M. Kang, A second-order-accurate symmetric discretization of the poisson equation on irregular domains, *J. Comput. Phys.* 176 (1) (2002) 205–227.
- [99] R.R. Nourgaliev, T.G. Theofanous, High-fidelity interface tracking in compressible flows: Unlimited anchored adaptive level set, *J. Comput. Phys.* 224 (2) (2007) 836–866.
- [100] X.-Y. Luo, M.-J. Ni, A. Ying, M. Abdou, Numerical modeling for multiphase incompressible flow with phase change, *Numer. Heat Transf. Part B Fundam.* 48 (5) (2005) 425–444.
- [101] R.P. Fedkiw, Coupling an Eulerian fluid calculation to a lagrangian solid calculation with the ghost fluid method, *J. Comput. Phys.* 175 (1) (2002) 200–224.
- [102] M. Sussman, A.S. Almgren, J.B. Bell, P. Colella, L.H. Howell, M.L. Welcome, An adaptive level set approach for incompressible two-phase flows, *J. Comput. Phys.* 148 (1) (1999) 81–124.
- [103] G. Son, N. Hur, A coupled level set and volume-of-fluid method for the buoyancy-driven motion of fluid particles, *Numer. Heat Transf. Part B Fundam.* 42 (6) (2002) 523–542.
- [104] D. Enright, R. Fedkiw, J. Ferziger, I. Mitchell, A hybrid particle level set method for improved interface capturing, *J. Comput. Phys.* 183 (1) (2002) 83–116.
- [105] Y. Zhang, Q. Zou, D. Greaves, Numerical simulation of free-surface flow using the level-set method with global mass correction, *Int. J. Numer. Methods Fluids* 63 (6) (2010) 651–680.
- [106] C. Frantzis, D. Grigoriadis, An efficient method for two-fluid incompressible flows appropriate for the immersed boundary method, *J. Comput. Phys.* 376 (2019) 28–53.
- [107] Y. Yap, H. Li, J. Lou, L. Pan, Z. Shang, Numerical modeling of three-phase flow with phase change using the level-set method, *Int. J. Heat Mass Transf.* 115 (2017) 730–740.
- [108] M. Reimann, Wärmeübergang bei freier Konvektion und Filmsieden: Allgemeines theoretisches Besprechungsverfahren und experimentelle Überprüfung im kritischen Gebiet, 1975.
- [109] E.R. Hosler, Film boiling on a horizontal plate, *ARS J.* 32 (4) (1962) 553–558.
- [110] P. Berenson, Experiments on pool-boiling heat transfer, *Int. J. Heat Mass Transf.* 5 (10) (1962) 985–999.
- [111] V. Klimenko, A. Shelepen, Film boiling on a horizontal plate—a supplementary communication, *Int. J. Heat Mass Transf.* 25 (10) (1982) 1611–1613.
- [112] P.J. Berenson, Film-boiling heat transfer from a horizontal surface, *J. Heat Transf.* 83 (3) (1961) 351–356.
- [113] M.T. Lebon, C.F. Hammer, J. Kim, Gravity effects on subcooled flow boiling heat transfer, *Int. J. Heat Mass Transf.* 128 (2019) 700–714.